NONLINEAR ULTRASONIC PHASED ARRAY IMAGING OF PARTIALLY-CLOSED FATIGUE CRACKS

A Thesis
Presented to
The Academic Faculty

by

Miralem Saljanin

In Partial Fulfillment
of the Requirements for the Degree
Master of Science in Engineering Science and Mechanics in the
School of Civil and Environmental Engineering

Georgia Institute of Technology
December 2017

NONLINEAR ULTRASONIC PHASED ARRAY IMAGING OF PARTIALLY-CLOSED FATIGUE CRACKS

Approved by:

Professor Laurence J. Jacobs, Advisor
School of Civil and Environmental Engineering
Georgia Institute of Technology

Dr. Jin-Yeon Kim
School of Civil and Environmental Engineering
Georgia Institute of Technology

Dr. Jianmin Qu
Department of Civil and Environmental Engineering
Northwestern University

Date Approved: 12 August 2017

ACKNOWLEDGEMENTS

The experience of both studying at one of the worlds best Universities and living in the U.S. for one year was amazing in every sense of the word! I would like to take this chance and express my deepest appreciation to all the great people who made this year unforgettable for me.

First and foremost, I would like to express my sincere gratitude to my adviser Professor Laurence J. Jacobs who made it even possible for me to study at GaTech, write a master's thesis in his lab and earn a M.Sc. degree in "Engineering Science and Mechanics". Thank you so much Larry for providing a familiar atmosphere in the lab, for the time you took not only talking with me about academic issues but also for your motivating and enlightening advices in exhausting times and last but not least for the numerous dinner invitations and ice cream runs.

Also, I absolutely want to thank Dr. Jin-Yeon Kim for his untiring support. His brilliant ideas and his outstanding comprehension in the field of wave propagation were fundamental for my master's thesis. Thank you Dr. Kim, your amazing personality made working with you in the lab a great experience!

Special thanks to David Moore and Ciji Nelson who provided our lab with the necessary instrumentation and who taught me the extensive handling with the OmniScan.

Furthermore, I want to thank my exchange partners Steffen Maier and Timm Geibel who became close friends and who made my stay in the U.S. so much more enjoyable. Thank you for the great time and the valuable memories! Also, I would like to thank my lab mates Gun Kim, David Torello, Katie Scott and Brian Fuchs for the great time I had with you in the lab.

Moreover, I would like to express my special thanks to Professor Michael Hanss and Dennis Schurr from the Institute of Engineering and Computational Mechanics at the University of Stuttgart and Sibylle Langer from the center of international affairs at the University of Stuttgart for choosing me as a candidate for this exchange program, which is financially supported by the German Academic Exchange Service DAAD. Therefore, I would also like to thank the DAAD for financially supporting me with its scholarship.

Finally, I want to express my utmost gratefulness towards my family for all their love and support, especially my parents who believed in me and encouraged me throughout my time at GaTech.

TABLE OF CONTENTS

LIST OF TABLES

LIST OF FIGURES

LIST OF SYMBOLS OR ABBREVIATIONS

∂	partial derivative operator
δ	variational operator
W	external work
U	internal energy
δU_0	strain density variation
f_i	body force vector
u_i	displacement vector
$\ddot{u}_i$	second time derivative of the displacement u_i
V	volume
S	surface or uniform grid size
$\sigma_i j$	stress tensor
n_j	normal vector
ϵ_{ij}	strain tensor
D	Diffraction loss
D_{ijkl}	higher order stiffness tensor
ρ_0	density of an undeformed body
ρ	density of an deformed body
t	time
s	distance
v	velocity
f	frequency
b_i	body forces
t_i	surface traction
E	Young's modulus
ν	Poisson ratio

λ	wavelength or first Lamé constant
μ	second Lamé constant
∇	Nabla operator
Ψ	zero-divergence vector potential
c_S	shear wave phase velocity
c_D	compression wave phase velocity
x_i	i, j, k axis or direction in coordinate system
$\vec{p}$	propagation vector
$\vec{d}$	particle motion vector
A, A_n	Amplitude
e	exponential function
k	wave number
w	angular frequency
θ_c	critical incident angle
F_ij	deformation gradient tensor
P_ij, j	Piola-Kirchhoff stress tensor
E_ij	Lagrangian strain tensor
O	Higher order terms
C_ijkl	second order elastic constant
C_ijkl	third order elastic constant
β	nonlinearity parameter
$\beta(\vec{r})$	nonlinearity metric
$E_H(\vec{r})$	higher load signal
$E_L(\vec{r})$	lower load signal
$V(k_x)$	spatial Fourier transform of the velocity field
D, D_b, D_s	directivity function
x_i	Eulerian coordinate

X_i	Lagrangian coordinate

SUMMARY

Phased array ultrasound is a highly advanced technique that is not only used in the nondestructive evaluation (NDE) of defects in materials but also in the medical diagnostic, for instance, e.g. for a noninvasive examination of the heart. However, difficulties occur in NDE applications when it comes to monitoring some challenging (nonlinear) defects such as small fatigue cracks in the early stages or partially- or fully- closed cracks. Small cracks may be undetected or sizes of closed cracks may be underestimated. The aim of this research is to obtain images of the closed part of a fatigue crack using the nonlinear ultrasonic phased array method. The present technique is based on a subtraction of response signals received at a sufficiently high and low energy level.

In this study, the essential experiments are performed on an aluminum CT specimen of 15 mm thickness that has a fatigue crack of 25 mm length and a Plexiglas specimen of 50 mm thickness. The crack in the Plexiglas specimen was produced by stretching the initial notch width of 2 mm to a final width of 2.5 mm. In order to investigate and evaluate these cracks, a commercial phased array system, with a 16 element probe operating at a frequency of 1.5 MHz, is used. The image of the crack tip is successfully generated by post-processing of the received signals at two excitation levels. The results clearly demonstrate the efficiency of the presented method to detect and image nonlinear defects.

CHAPTER I

INTRODUCTION

1.1 Motivation and Objective

Nondestructive evluation (NDE) has evolved into a very interdisciplinary field of research with a broad spectrum of applications not only in industry - for the examinations of materials and structures - but also in the medical field, where ultrasonic waves are used for a noninvasive examination of organs. Due to numerous advantages of ultrasonic methods, such as the possibility of fast, safe and inexpensive investigations, they became to one of the most frequently used techniques in the field of NDE [15]. In ultrasonic NDE, beams of high frequency elastic waves are fed into the specimen for the detection of discontinuities in the material. The propagation of sound waves is associated to a loss of energy (attenuation) and a partial reflection at interfaces. Therefore, methods using ultrasonic waves are able to detect defects in materials by monitoring changes in the characteristics of the wave propagation including [25]

- reflections of the wave caused by surfaces consisting of material boundaries or by flaws within the material itself.
- attenuation of the propagating wave due to scattering and absorption within the specimen.

However, ultrasonic methods reach their limitations when it comes to monitoring (nonlinear) cracks such as partially or fully closed cracks or cracks in the early stages. Why it is important to study the initiation of cracks can be illustrated by the following example. On May 2, 1953, the British-made aircraft de Havilland Comet G-ALYV

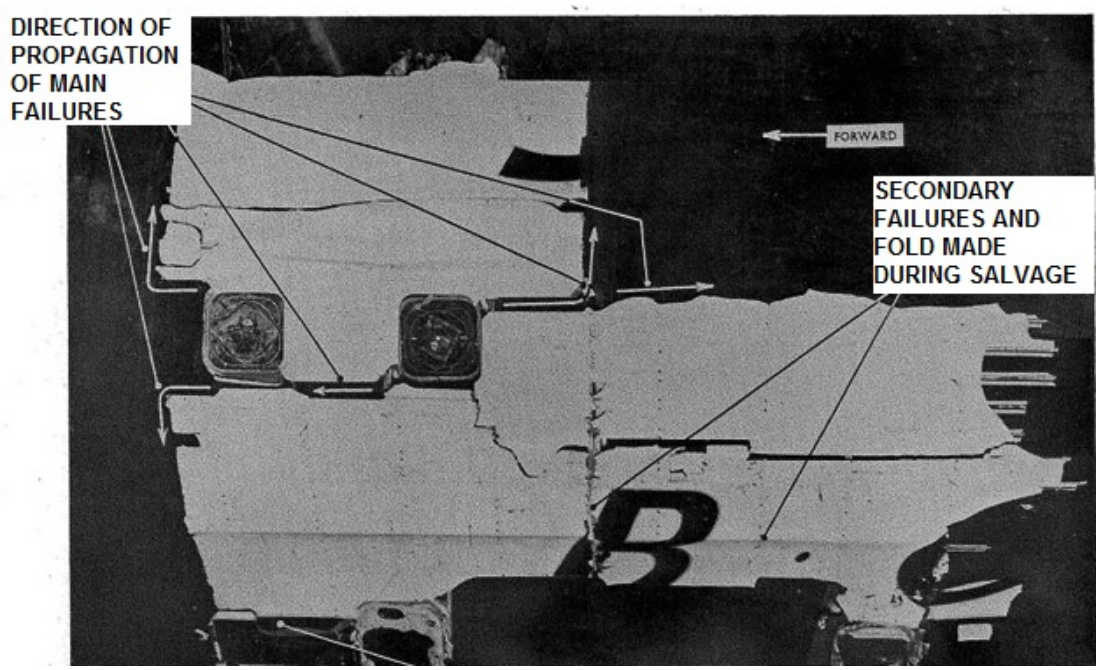

Figure 1: Original wreckage of the Comet G-ALYP. This piece was determined to be the origin of the in-flight break-up [1].

crashed into the ground, six minutes after take off. On January 10, 1954, Comet G-ALYP fall into the sea in flames, 20 minutes after take-off. On April 8, 1954, Comet G-ALYY experienced an in-flight break-up and crashed into the sea, just 40 minutes after take-off. As a result of three catastrophic accidents in less than a year, by planes manufactured by the same company, investigations on the cause of the plane crashes have been ordered. After this investigation the definition of a "fatigue crack" hit the headlines for the first time. Scientists were able to determine that two main failures led to these accidents. First, the airplanes had squarish windows and secondly, the supporters around the windows were riveted, not glued, which created undetectable cracks in the material. The stretching and tightening of the pressurized cabin in combination with changing strain caused a growth of the small cracks, along the edges of the windows (Fig. 1). In the course of time, the crack growth finally reached a size which led to a total collapse of the airplane structure.

In this research the detection of such cracks in the early stages - using nonlinear

ultrasonic phased arrays - is studied. Compared to classical NDE techniques, nonlinear ultrasound offers high potential for enabling a qualitative evaluation of defects in structures and materials even before the initiation of the first crack.

Previous research has demonstrated that nonlinear ultrasound is sensitive to microstructural changes [27], [19], [30]. First applications of nonlinear ultrasound were predominantly performed to quantify crack damages while more recent research focuses on the analysis of the true depth of a crack, as examined by Cheng in [14]. Potter et al. presented a nonlinear imaging method based on the normalized difference between the sequential and parallel transmission energies [26]. However, this research will examine a nonlinear imaging method based on the subtraction of response signals as presented by Ohara et al., similarly [32], [33], [18], [5], [31], [2], [34], [3].

The objective of this research is to examine a nonlinear ultrasonic phased array imaging method based on the subtraction of signals received at two different energy levels. For this purpose, a commercial phased array system (OmniScan, Model MX2, Olympus), along with a 16 element probe operating at a frequency of 1.5 MHz, is used.

1.2 Structure of Thesis

In order to understand the physics behind the linear as well as the nonlinear wave propagation in elastic solids, an introduction to the fundamental theory will be given in the second chapter. Beside the derivation of the equations of motion, essential terms, such as wave scattering and attenuation will be described in detail. Thereupon, the main topic of this research - ultrasonic phased arrays - will be elaborated in chapter 3. For a solid understanding of the physics of phased array systems, the effects of phased pulsing of signals, such as beam steering and beam focusing will be described in the third chapter, too. At the end of this chapter it will be explained how both linear

and nonlinear images are created. For this purpose, the main idea behind this research - imaging the nonlinearity parameter $\beta(\vec{r})$ - will also be discussed. Afterwards, the experimental set-up, the instrumentation and the specimen will be introduced in chapter 4. The main part of this research, the analysis of the subtraction method by evaluating measurements at different crack sizes, which covers a post-processing of the received signals in Matlab, will be discussed in chapter 5. With the aid of these images a conclusion about the efficiency of the presented imaging method can be drawn in chapter 6.

CHAPTER II

THEORETICAL BACKGROUND

In order to completely understand the physics behind this research, a thorough explanation -based on Aschenbach [4]- of wave propagation theory will be given in this section. For this purpose both linear and nonlinear wave propagation in elastic solids will be discussed. To begin with, the general equations of motion for a linear and isotropic medium is going to be derived in terms of the displacement. Afterwards, the propagation of plane harmonic waves in linear elastic materials will be the focus of the discussion. Since the theory of nonlinear wave propagation is essential for this research, the assumption of linear elasticity is dropped and the fundamental ideas of nonlinear wave propagation is presented in the last part of this chapter.

2.1 Wave Propagation

In this section, the essential aspects of wave propagation, such as the equations of motion or wave characteristics like reflection and transmission in elastic solids will be described in detail. However, it is necessary to give a definition for elastic materials at this point before going further in detail. Elastic materials are characterized by their correspondence between stress and strain, which means that during loading and unloading such materials follow the same stress-strain path. Therefore, the strain density function U_0 can be described, independently of the strain history, only in terms of the current strain state [11].

However, for materials with no energy dissipation (conservative materials) we can formulate the relation

$$\delta W = \delta U \tag{1}$$

δW describes the external work done on the material and δU represents the variation of internal energy of the material. Therefore, this equation means that the external work on the material has to be equal to the total change in the strain energy of the material. By applying the following relations and the divergence theorem on the surface integral

$$\delta W = \int_V f_i \delta u_i \, \mathrm{d}V + \int_S t_i \delta u_i \, \mathrm{d}S \qquad , \qquad \delta U = \int_V \delta U_0 \, \mathrm{d}V \tag{2}$$

where f_i describes the applied body force, t_i the surface traction

$$t_i = \sigma_{ij} n_j \tag{3}$$

and δU_0 the strain density variation, equation (1) can be reformulated by using the divergence theorem on the surface integral as follows:

$$\begin{aligned}
\int_V \delta U_0 \, \mathrm{d}V &= \int_V f_i \delta u_i \, \mathrm{d}V + \int_V \left(\sigma_{ij} \delta u_i\right)_{,j} \mathrm{d}V \\
&= \int_V f_i \delta u_i \, \mathrm{d}V + \int_V \left(\sigma_{ij,j} \, \delta u_i + \sigma_{ij} \delta u_{i,j} \right) \mathrm{d}V \\
&= \int_V \left(f_i \delta u_i + \sigma_{ij,j} \, \delta u_i + \sigma_{ij} \delta u_{i,j} \right) \mathrm{d}V \\
&= \int_V \left(\left(f_i + \sigma_{ij,j} \right) \delta u_i + \sigma_{ij} \delta u_{i,j} \right) \mathrm{d}V
\end{aligned} \tag{4}$$

Equation (3) can be simplified with the aid of the force equilibrium for an cubic element

$$\sigma_{ij,j} + f_i = 0 \tag{5}$$

Applying equation (4) we receive the equation

$$\begin{aligned}
\int_V \delta U_0 \, \mathrm{d}V &= \int_V \left(\sigma_{ij} \delta u_{i,j} \right) \mathrm{d}V \\
&= \int_V \frac{1}{2} \left(\delta u_{i,j} + \delta u_{j,i}\right) \mathrm{d}V \\
&= \int_V \sigma_{ij} \delta \epsilon_{ij} \, \mathrm{d}V.
\end{aligned} \tag{6}$$

Due to the fact that equation (5) is valid for every voluminous element, the following relation between the strain density U_0 and the strain ϵ_{ij} can be derived

$$\delta U_0 = \sigma_{ij} \delta \epsilon_{ij} \tag{7}$$

where U_0 is assumed to be a polynomial of the form

$$U_0 = D_0 + D_{kl}\epsilon_{kl} + D_{klmn}\epsilon_{kl}\epsilon_{mn} \tag{8}$$

Considering the definition of elastic materials, equation (6) can be reformulated as

$$\begin{aligned}
\sigma_{ij} &= \frac{\partial U_0}{\partial \epsilon_{ij}} \\
&= D_{kl}\delta_{ik}\delta_{jl} + D_{klmn}\left(\delta_{ik}\delta_{jl}\epsilon_{mn} + \epsilon_{kl}\delta_{im}\delta_{jn}\right) \\
&= D_{ij} + D_{ijmn}\epsilon_{mn} + D_{klij}\epsilon_{kl} \\
&= D_{ij} + \left(D_{ijkl} + D_{klij}\right)\epsilon_{kl}.
\end{aligned} \tag{9}$$

Finally, the linear relation between stress and strain of elastic materials

$$\sigma_{ij} = C_{ijkl}\epsilon_{kl} \tag{10}$$

is obtained with $(D_{ijkl} + D_{klij}) = C_{ijkl}$ and $D_{ij} = 0$, where C_{ijkl} describes the fourth order stiffness tensor.

2.1.1 Equations of Motion

The derivation of the equation of motions follows from the laws of mechanics and must fulfill Newton's first law in particular. Therefore, the equations of motions can be derived by considering a voluminous element V, bounded by the surface S, at time t. Due to the momentum principle, the instantaneous rate of change of the total momentum of all particles is equal to the sum of all external forces. Hence, the equilibrium of moments can be written as

$$\int_V \rho b_i \,\mathrm{d}V + \int_S t_i \,\mathrm{d}S = \int_V \rho \ddot{u}_i \,\mathrm{d}V \tag{11}$$

where ρ describes the density of the material, b_i the body forces and t_i the surface traction. $\ddot{u}_i$ represents the second time derivative of the displacement u_i. By using the Cauchy stress definition

$$t_i = \sigma_{ij} n_j \tag{12}$$

we can substitute t_i in equation (11) to receive

$$\int_V \rho b_i \, \mathrm{d}V + \int_S \sigma_{ij} n_i \, \mathrm{d}S = \int_V \rho \ddot{u}_i \, \mathrm{d}V \tag{13}$$

Cauchy's first law of motion can be obtained by applying the divergence theorem

$$\int_S \sigma_{ij} n_i \, \mathrm{d}S = \int_V \sigma_{ij,i} \, \mathrm{d}V \tag{14}$$

in equation (13). Note that the stress tensor σ_{ij} is symmetric. Cauchy's first law of motion can be written as

$$\int_V (\sigma_{ij,i} + \rho b_j - \rho \ddot{u}_j) \, \mathrm{d}V = 0 \tag{15}$$

Since equation (15) has to hold for any arbitrary volume, it follows that

$$\rho \ddot{u}_j = \sigma_{ij,j} + \rho b_i \tag{16}$$

Furthermore, the stress-strain relationship for homogeneous and isotropic solids in equation (10) can be reformulated as

$$\sigma_{ij} = \lambda \epsilon_{kk} \delta_{ij} + 2\mu \epsilon_{ij} \tag{17}$$

by using Young's modulus E and the Poisson ratio v

$$\lambda = \frac{Ev}{(1+v)(1-2v)} \qquad , \qquad \mu = \frac{E}{2(1+v)} \tag{18}$$

In equation (17), the strain tensor ϵ is given in the linearized form of the strain-displacement relation

$$\epsilon_{ij} = \frac{1}{2}(u_{i,j} + u_{j,i}) \tag{19}$$

Navier's equations of motion can be derived by applying equation (17) and (19) in (16) and neglecting the body forces. This yields in tensorial notation

$$\rho\ddot{u_j} = (\lambda + \mu)u_{i,ij} + \mu u_{j,ii} \tag{20}$$

which can be written with vector notation as

$$\rho\ddot{\vec{u}} = (\lambda + \mu)\nabla\nabla \cdot \vec{u} + \mu\nabla^2\vec{u} \tag{21}$$

By using the vector identity $-\nabla \times \nabla \times \vec{u} + \nabla\nabla\vec{u} = \nabla^2\vec{u}$ equation (21) can be obtained in terms of

$$\rho\ddot{\vec{u}} = (\lambda + 2\mu)\nabla\nabla\cdot\vec{u} - \mu\nabla^2\vec{u} \tag{22}$$

Moreover, equation (22) can be separated into a solution for a shear wave (SV-wave) and a compression wave (P-wave) by introducing the Helmholtz decomposition of the displacement vector $\vec{u}$ [9],

$$\vec{u} = \nabla\Phi + \nabla \times \vec{\Psi} \tag{23}$$

where the gradient of the scalar Φ and the rotation of the zero-divergence vector potential Ψ is used to separate the P-wave and the SV-wave. This is only possible due to the fact that the linear case is regarded and the principle of superposition is valid. Furthermore, the additional constraint $\nabla \cdot \Phi = 0$ is necessary to guarantee a unique solution. With the Helmholtz decomposition it is possible to study partial differential equations in both space and time. By using the mathematical identity $\nabla \times \Phi = 0$ for any scalar Φ equation (23) can be solved for the shear wave as follows:

$$\rho\frac{\partial^2(\nabla \times \vec{u})}{\partial t^2} = \mu\nabla^2(\nabla \times \vec{u}) \tag{24}$$

where $\vec{\Psi} = \nabla \times \vec{u}$ can be substituted in equation (24) to receive the simplified equation

$$\nabla^2\vec{\Psi} = \frac{1}{c_S^2}\frac{\partial^2}{\partial t^2}\vec{\Psi} \tag{25}$$

where c_S describes the shear wave phase velocity

$$c_S = \sqrt{\frac{\mu}{\rho}} \tag{26}$$

Similarly, by using the mathematical identity $\nabla \cdot (\nabla \times \vec{x}) = 0$ equation (23) can be solved for the P-wave equation as follows:

$$\rho \frac{\partial^2 (\nabla \vec{u})}{\partial t^2} = (\lambda + 2\mu) \nabla^2 (\nabla \cdot \vec{u}) \tag{27}$$

Substituting $\Psi = \nabla \cdot \vec{u}$, the wave equation for the P-wave can be reformulated in terms of

$$\nabla^2 \Phi - \frac{1}{c_D^2} \frac{\partial^2}{\partial t^2} \Phi = 0 \tag{28}$$

where c_D describes the phase velocity of the compression wave

$$c_D = \sqrt{\frac{\lambda + 2\mu}{\rho}} \tag{29}$$

2.1.2 Linear Wave Propagation

Since the essential equations of motion were derived in the previous section, the fundamentals of linear wave propagation will be discussed in the following paragraphs, where both the P- and the S-wave will be explained as well as their transmission and reflection at a stress free surface. However, only plane waves are discussed in the following.

2.1.2.1 Plane Waves

Wave phenomena as a result of the derived wave equations will be presented in this section. A plane wave is a wave of constant frequency whose wave fronts occur on infinite parallel planes, which implies that on each of these planes the waves adopt a constant value for the displacement u, the stress σ and the strain ϵ. In fact, it is technically not possible to generate such a wave but it is a good approximation for many waves. By using this approximation, many phenomena of wave propagation

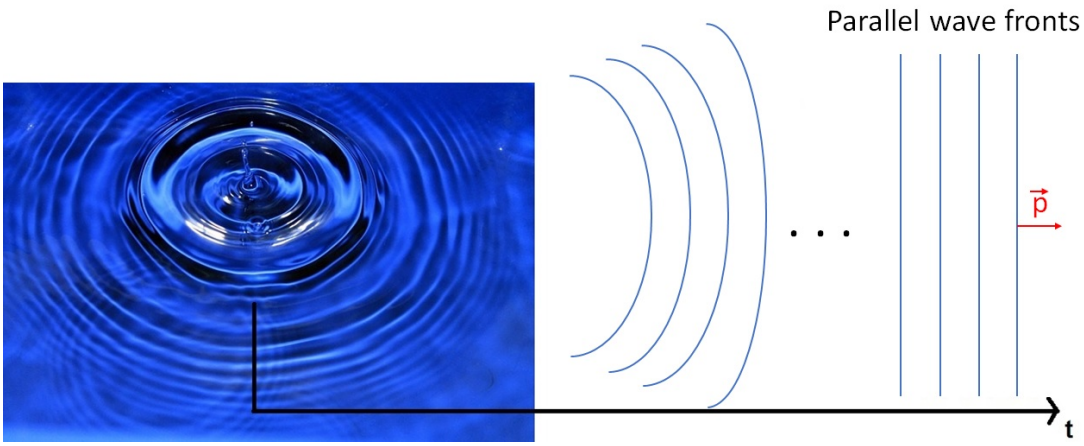

Figure 2: waterdrop wavefronts in the distance as an example of plane waves [20].

can be expressed pretty easily for plane waves. The normalized vector perpendicular to these planes is assigned as the unit propagation vector p. The wave fronts of a drop in the water can be approximately used to illustrate a plane wave by looking at the wave fronts in a distance far enough away from the wave emitting source (Fig. 2). However, for the upcoming discussion a wave propagation in an isotropic and homogeneous solid will be considered. Under this assumption, the displacement vector u can be mathematically described by

$$\vec{u} = f(x \cdot \vec{p} - ct)\vec{d} \tag{30}$$

due to a propagation of a plane wave with velocity c in the direction of the unit vector $\vec{p}$. Here, the velocity c can be both the shear wave velocity c_S or the compression wave velocity c_D. In this equation, the normalized unit particle motion vector d is a vector pointing in the direction in which a single particle is displaced. By substituting equation (30) into equation (21) the following equation can be obtained, which is known as Navier's equation for plane waves:

$$(\mu - \rho c^2)\vec{d} + (\lambda + \mu)(\vec{p} \cdot \vec{d})\vec{p} = 0 \tag{31}$$

However, this equation can just be satisfied for perpendicular or parallel vectors $\vec{p}$ and $\vec{d}$. Therefore, we can only formulate two possible solutions for Navier's equation

for plane waves [28].

1. $\vec{p}$ and $\vec{d}$ are perpendicular. In this case a shear wave/S-wave is considered propagating perpendicular to the direction of the particle motion, which implies that $\vec{p} \cdot \vec{d} = 0$. Considering a wave propagating in a two-dimensional plane it can either have an in-plane displacement (SV-wave) or and out-of-plane displacement (SH-wave). Nevertheless, solving Navier's equation (30) for the wave velocity c yields for both cases $c = c_S$ as formulated in equation (26)

2. $\vec{p}$ and $\vec{d}$ are parallel. In this case a longitudinal wave/P-wave is considered propagating in the same direction as the particle motion, which implies that $\vec{p} = \pm\vec{d}$. Solving Navier's equation (30) for the wave velocity c the longitudinal wave velocity $c = c_D$ in equation (29) can be obtained.

Since $\sqrt{\frac{\lambda+2\mu}{\rho}} > \sqrt{\frac{\mu}{\rho}}$ it can be concluded that for all elastic solids the longitudinal wave velocity c_L is higher than the shear wave velocity c_D. A special form of plane waves are harmonic ones for which the equation for the displacement u can be formulated as

$$\vec{u} = A\vec{d}e^{i \cdot k(x \cdot \vec{p} - ct)} \tag{32}$$

where A describes the complex amplitude of the wave depending neither on x nor on t. $k = \frac{w}{c}$ is the wave-number with $w = 2\pi f$ being the angular frequency.

2.1.2.2 Reflection of a Plane Wave at a Stress Free Surface

For the above derived wave equations it is assumed that the waves independently propagate in an infinite medium, although in reality ultrasound applications involve the interaction of waves propagating in finite media with boundaries generating reflection and transmission. However, since the following discussion will be based on a reflection of plane waves at a stress free surface, an idealized case of a boundary between a medium and vacuum, e.g. idealized air, will be considered. Aschenbach [4]

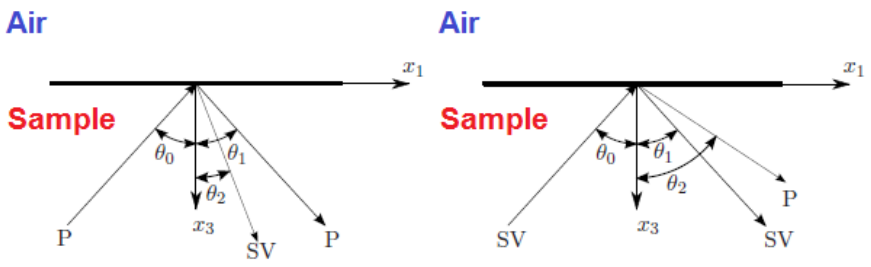

Figure 3: Reflection of a longitudinal or shear wave at a stress free surface [16]

describes the displacement - in the two dimensional case - of a longitudinal or shear wave as follows

$$\vec{u} = A_n \vec{d}^{(n)} e^{ik_n(x_1 p_1^{(n)} + x_2 p_2^{(n)} - c_n t)} \tag{33}$$

where A_n describes the amplitude of the propagating wave. The index n is used to differentiate between a longitudinal wave and vertically polarized shear wave (SV-Wave) propagating in the (x_1, x_3)-plane. In contrast to vertically polarized waves propagating only in the (x_1, x_3)-plane excluding the x_2-direction, there are also horizontally polarized shear waves (SH-Waves) propagating only in the (x_1, x_2)-plane excluding the x_3-direction. However, both waves are propagating in the (x_1, x_3)-plane with the boundary perpendicular to the x_2-axis. Fig. 3 exemplifies an incident P- and SV-wave for two different cases at a stress free boundary. The angle under which the reflected P- or SV-wave propagate depends on the angle of the incident wave θ_0. In fact, if $\theta_0 = 0$ the incident P- or SV-wave hits the boundary orthogonal, which results in a reflection of only one wave that is the same as the incident wave. If $\theta_0 > \theta_c$, where θ_c is the critical incident angle defined by Snell's Law as $\theta_c = arcsin(\frac{c_S}{c_D})$, the P-wave will propagate along the surface as a so-called "Rayleigh surface wave". Therefore, there will just be a reflected SV-wave in this case.

In order to derive a correlation between the angles θ_0, θ_1 and θ_2, which is shown in Table 2, equation (32) can be used additionally to the fact that ω doesn't change

Incident θ_0	**Reflected θ_1**	**Reflected θ_2**
Incident SV-Wave	$sin(\theta_1) = \frac{c_D}{c_S} \cdot sin(\theta_0)$	$\theta_2 = \theta_0$
Incident P-Wave	$\theta_1 = \theta_0$	$sin(\theta_2) = \frac{c_S}{c_D} \cdot sin(\theta_0)$

Table 2: Relations between θ_0, θ_1 and θ_2 for a reflection at a stress free surface

after reflection. For the amplitudes A_n $(n = 1, 2, 3)$, the angles have to satisfy the following relation

$$k_0 sin(\theta_0) = k_1 sin(\theta_1) = k_2 sin(\theta_2) \tag{34}$$

which is known as Snell's law. This is so in order to receive a non-trivial solution for the amplitudes A_n.

2.1.3 Nonlinear Wave Propagation

The goal of this section is to briefly describe the theory of nonlinear wave propagation, especially with regard to the differences to linear wave theory. A rigorous derivation of nonlinear wave equations can be found in [17]. In the linear case the wave propagates at a constant frequency, the excitation frequency. In contrast to that, the propagating wave for the nonlinear case travels with changing frequency content due to material nonlinearities, such as defects or irregularities in the material structure (Fig. 4). These additional frequencies are referred as higher harmonics which are multiples of the fundamental frequencies.

However, when talking about material nonlinearities it has to be differentiated between a damage induced or inherent (natural) cause of the nonlinearity. For instance, dislocations or fatigue cracks are damage induced nonlinearities whereas vacancies in the crystal lattices are considered as inherent ones.

For the derivation of nonlinear wave equations it is more convenient to express the stress-strain relation using Lagrangian coordinates instead of Eulerian ones [8]. The relationship between Lagrangian and Eulerian coordinates is given by the deformation

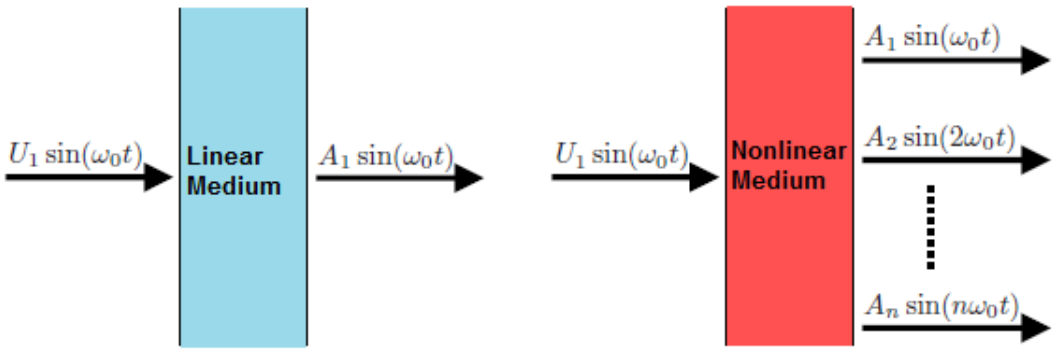

Figure 4: Difference between linear and nonlinear wave propagation [8] [6]

gradient tensor

$$F_{ij} = \frac{\partial x_i}{\partial X_j} \tag{35}$$

where X describes the Lagrangian coordinate frame and x the Eulerian frame. As a first step towards further derivations it is necessary to formulate the balance of linear momentum in Lagrangian coordinates,

$$P_{ij,j} = \rho_0 \frac{\partial^2 u_i}{\partial t^2} \quad , \tag{36}$$

where $P_{ij,j}$ denotes the Piola-Kirchhoff stress tensor

$$P_{ij,j} = \frac{\rho_0}{\rho} \sigma \cdot F_{ij}^{-T} \quad , \tag{37}$$

and ρ_0 and ρ describe the density of the undeformed and deformed body, respectively. With this tensor, equation (16) can be transformed into Lagrangian coordinates as

$$P_{ij,j} = \rho_0 \ddot{u}_i \tag{38}$$

while still neglecting body forces. For elastic materials the specific strain energy per unit mass W is given by

$$P_{ij} = \rho_0 \frac{\partial W}{\partial F_{ij}} \tag{39}$$

However, $W = W(E)$ since for most materials it can be assumed that W only depends on the local stretching and volume change. Therefore, the Piola-Kirchhoff stress can

be formulated in terms of the strain energy W as

$$P_{ij} = \rho_0 F_{ij} \frac{\partial W}{\partial E_{ij}} \tag{40}$$

where E_{ij} denotes the Lagrangian strain tensor

$$E_{ij} = \frac{1}{2}\left(\frac{\partial u_i}{\partial X_j} + \frac{\partial u_j}{\partial X_i} + \frac{\partial u_k}{\partial X_i}\frac{\partial u_k}{\partial X_j}\right). \tag{41}$$

Furthermore, for the strain energy W a power series expansion can be used for small strains which leads to

$$\rho_0 W = \frac{1}{2!} C_{ijkl} E_{ij} E_{kl} + \frac{1}{3!} C_{ijklmn} E_{ij} E_{kl} E_{mn} + O. \tag{42}$$

In this equation, C_{ijkl} and C_{ijklmn} describe the second and third order elastic constants. Higher order terms, which can be neglected under the assumption of small strains, are denoted by O. However, by using the symmetry of the strain tensor E_{ij}, equation (40) can be formulated as

$$P_{ij} = C_{ijkl}\frac{\partial u_k}{\partial x_l} + \frac{1}{2} D_{ijklmn}\frac{\partial u_k}{\partial x_l}\frac{\partial u_m}{\partial x_n} \quad , \tag{43}$$

where the second and third order elastic coefficients are summarized in

$$D_{ijklmn} = C_{ijklmn} + C_{ijln}\delta_{km} + C_{jnkl}\delta_{im} + C_{jlmn}\delta_{ik} \tag{44}$$

Finally, the nonlinear differential equation for the displacement u

$$\rho_0 \ddot{u}_i = \frac{\partial^2 u_k}{\partial x_j \partial x_l}\left(C_{ijkl} + D_{ijklmn}\frac{\partial u_m}{\partial x_n}\right) \tag{45}$$

is received by plugging equation (43) into (38), which can be further simplified to

$$\ddot{u} = \frac{\partial^2 u}{\partial x^2} \cdot A + \frac{\partial^3 u}{\partial x^3} \cdot B \tag{46}$$

Here, A and B are coefficients depending on the second order elastic coefficient C_{ijkl} and on a combination of C_{ijkl} as well as the tensor D_{ijklmn}, respectively. On the basis of Kim [13] a solution to equation (46) can be written as

$$u(X,t) = \underbrace{u_0}_{A_1} \cdot \sin(kX - t) - \underbrace{\underbrace{\frac{Bk^2}{8A}{u_0}^2 X}_{A_2} \cos(2(kX - t)) \quad + O}_{\text{wave equation for the second harmonic}} \quad , \tag{47}$$

where again O denotes higher order terms which can be neglected.

2.1.3.1 Nonlinearity Parameter β

In this section, an absolute nonlinearity parameter β will be derived which is an absolute and material (undamaged) related value. This parameter β is a quantitative representation for the degree of nonlinearity in materials. However, an increase in the β-value is observable as a result of plastic deformation in materials [12]. On basis of the derived equations in the previous section, a mathematical expression for β will be derived in the following. Since this research is based on longitudinal measurements it is important to note that the upcoming formulations for β only hold for this kind of waves! According to [10] and [21] the accoustic nonlinearity is negligible in isotropic materials due to the symmetry between the moduli of the second and third order.

As already marked in equation (47) an expression for the amplitude of the second harmonic can be described by

$$A_2 = \frac{Bk^2}{8A} {u_0}^2 X \tag{48}$$

Defining the nonlinearity parameter as $\beta = \frac{B}{A}$ the equation for the second harmonic amplitude can be solved for β to receive the following equation:

$$\beta = \frac{A_2}{A_1^2} \cdot \frac{8}{k^2 X} \tag{49}$$

CHAPTER III

PHASED ARRAY ULTRASOUND

In order to understand the physics behind phased array systems, a thorough explanation -based on [29] - will be given in this section. For this purpose, the set-up of phased array systems will be described at the beginning. Afterwards, it will be discussed how beams can be generated, steered and focused to detect flaws in materials. In the last section of this chapter it will be shown how images of the received signals can be generated. Furthermore, the nonlinear imaging method used in this research, which is based on a subtraction of signals at two different energy loads, will be presented at the end.

3.1 Set-Up of Phased Array System

Usual ultrasonic transducers consist of either two separate elements for generating and receiving ultrasonic waves or just of one element for both generating and receiving the signals (Fig. 5). However, phased array probes consist of an assembly of elements which can be pulsed separately. Such a phased array probe consists of 16 up to 256 individual elements which can be arranged in different shapes (Fig. 6) [7]. The transducer frequencies of these probes are usually in the range of 1.5 MHz to 10MHz. As part of an angle beam assembly with a wedge, phased array probes may be designed for direct contact use (Fig. 7). On the other hand, they can also be used for immersion inspections with sound coupling through a water path. Last but not least, a computer-based device for driving the probes, pulsing and processing the receiving signals as well as imaging the signal information in different possible ways, is also an essential part of a phased array system (Fig. 8).

The biggest advantage of phased array systems over conventional flaw detectors

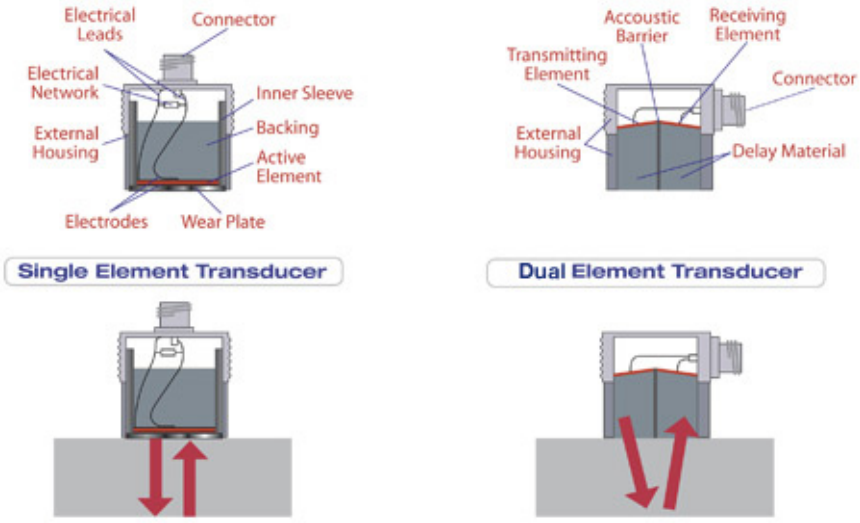

Figure 5: Difference between a single element transducer and a dual element one [22].

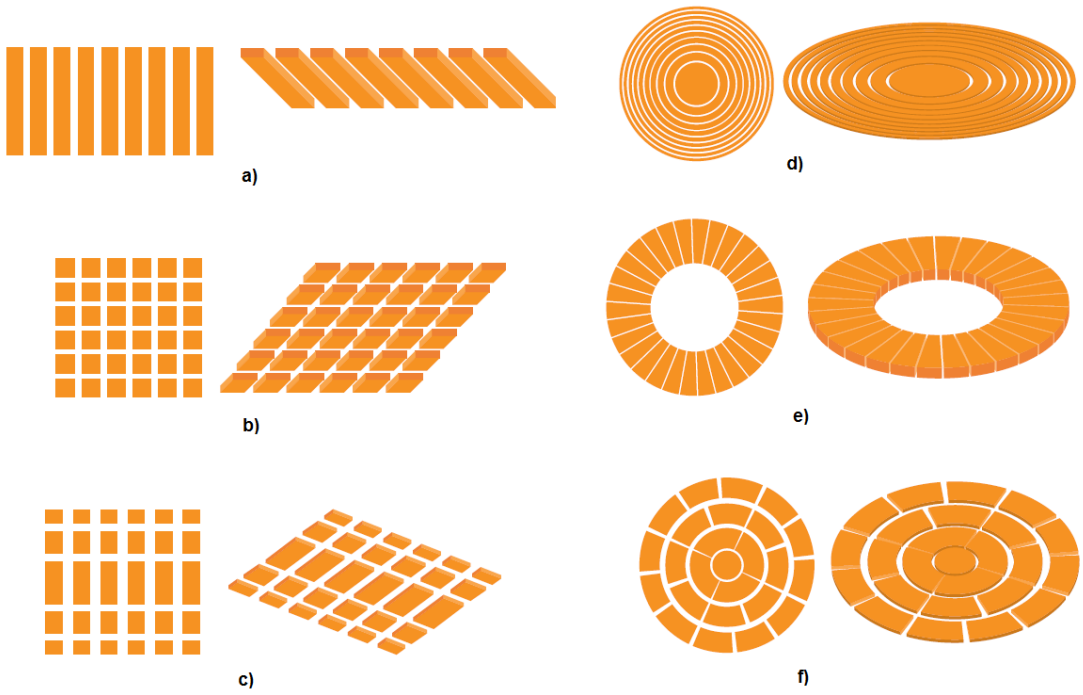

Figure 6: a) 1D linear phased array probe b) 2D matrix phased array probe c) 1.5D matrix phased array probe d) Annular phased array probe e) 1D circular phased array probe f) Segmented annular phased array probe [29]

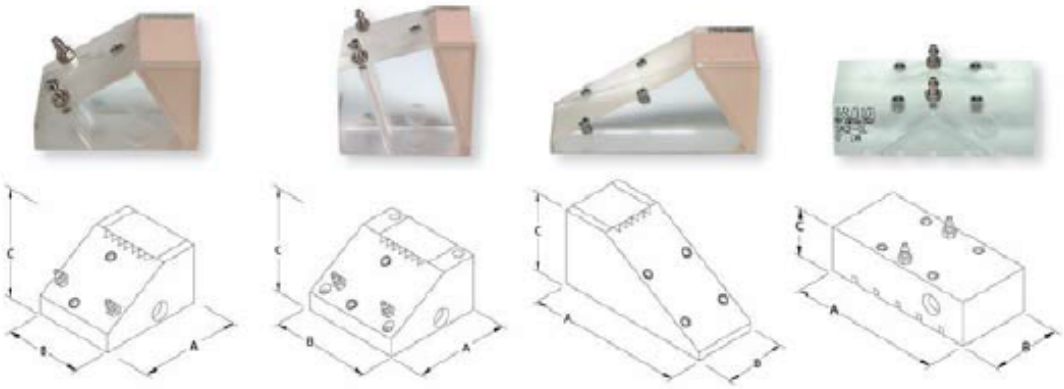

Figure 7: Wedges for phased array probes [29]

Figure 8: Commercial Phased Array System [24]

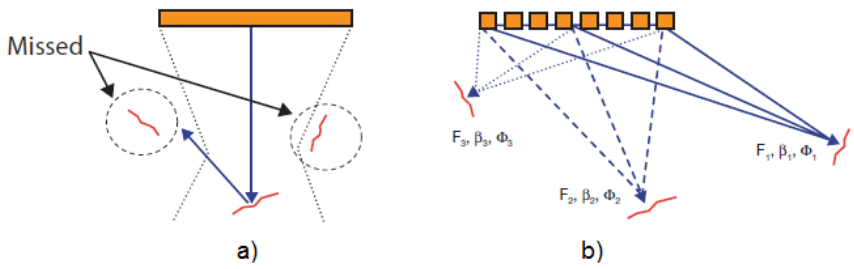

Figure 9: Detection of cracks with a) a single element probe and b) a phased array probe. In contrast to a) the beam of phased array probes are focused and multiangled enabling a crack detection of most orientations [29].

is the flexibility and capability in inspections due to the possibility of pulsing sound beams along a linear path, through a range of refracted angles or through focusing at specific spots at a different number of depths. Steering and focusing a beam is possible through pulsing waves successively with a short time delay. In the following section, the effects of phased pulsing will be explained in detail.

3.2 Effects of Phased Pulsing

As already mentioned in the previous section, most ultrasonic inspections use single or dual element transducer with divergent beams, where the waves propagate along an acoustic axis with a single refracted angle [29]. The disadvantage of this method is illustrated in Fig. 9a. However, each element in a phased array probe can be considered as a line source of cylindrical waves. By pulsing them separately, the single wave fronts will interfere and generate an overall wave front. In order to generate a focused beam with steering capability, the single wave fronts can be time-delayed and synchronized for amplitude and phase through a computer-controlled excitation of the individual elements in a phased array probe. With this technique it is possible to detect disoriented cracks (Fig. 9b). The principle of focusing and steering beams is illustrated in Fig. 10. At first, a trigger signal is sent from the acquisition to the phased array unit which transforms the signal into a high-voltage pulse. This pulse has a pre-programmed width and time delay. Since every single element in the probe

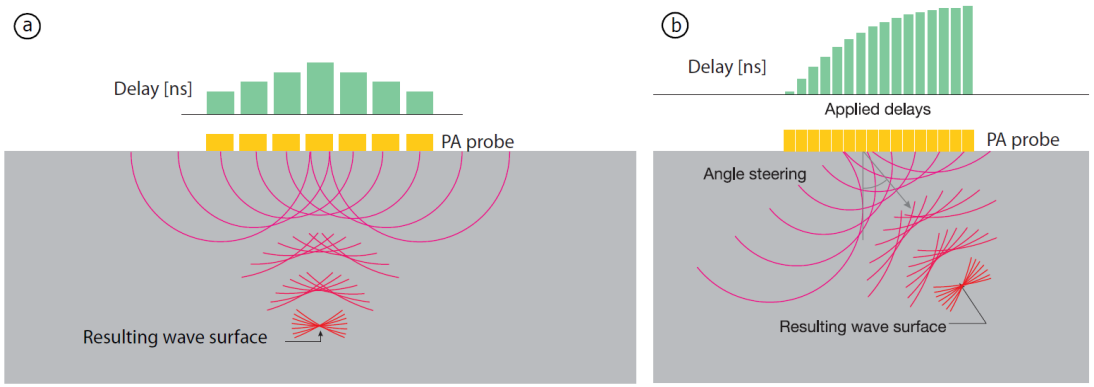

Figure 10: Principle of focusing and steering a beam by applying time delays. a) shows a beam with normal incidences whereas b) illustrates a beam with angled ones [29].

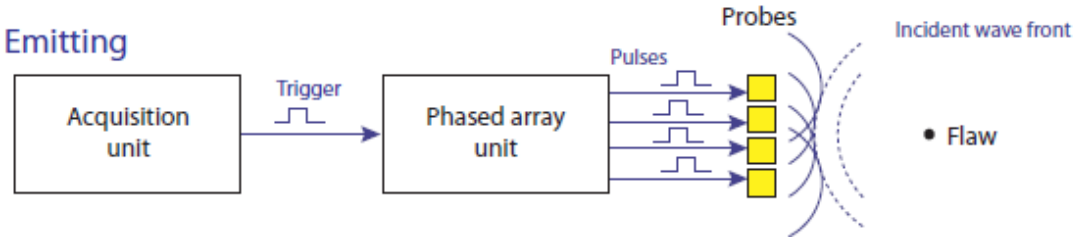

Figure 11: Pulsing the elements with a time delay to generate a beam [29].

receives only one pulse, a beam with a specific angle and depth can be generated (Fig. 11). However, by reaching a flaw in the material the beam bounces back and the acquisition unit can detect this defect in two steps. First, the received echo signals of the single elements have to be time-shifted back. Second, the echo signals have to be reunited to a single ultrasonic pulse that is sent back to the acquisition unit.

Moreover, the response of phased array probes is dependent on both the characteristic transducer parameters and the parameters of the excitation pulse. These parameters which are essential for shaping the beam will be explained in the following section.

3.2.1 Beam Shaping

Not only the frequency of phased array probes but also the number of elements, the element size, the pitch and the aperture are important transducer parameters.

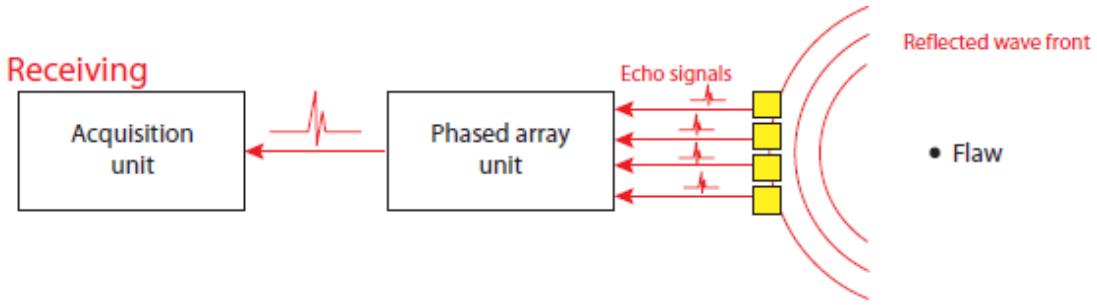

Figure 12: Detecting a flaw through time-shifting and summing the received echo signals [29].

In this research, an ultrasonic phased array probe with a frequency of 1.5 MHz was used. Due to the fact that higher frequency probes provide a better signal to noise ratio - because of sharper focusing - than lower frequency ones, a tighter and more optimized focal point could be achieved by using a higher frequency probe. However, the material attenuation of propagating waves will increase with higher frequencies resulting in a decrease in the penetration depth of the beam. Therefore, inspections of materials that are highly scattering or attenuating require the use of phased array probes with lower frequency rates.

Furthermore, a probe with 16 elements was used in this research. The advantage for using a probe with more elements lies in the fact that not only the coverage area is increased but also the steering and focusing capability of the beam.

Also, the element size e plays an important role for the shape of a beam (Fig. 13). The steering and focusing capability increase as the element size decreases. However, strong side lobes will appear if the the element size is less than one wavelength leading to a minimum size of 0.2 mm in commercial probes.

The pitch p is the distance between two elements. With a small value for p, the steering range can be further optimized. The effective size of a pulsing element is called the aperture A. The (virtual) aperture is usually comprised of a group of up to 16 individual elements that are pulsed at the same time (Fig. 14). For inspections with high sensitivity and a low beam spreading as well as optimal focusing capabilities

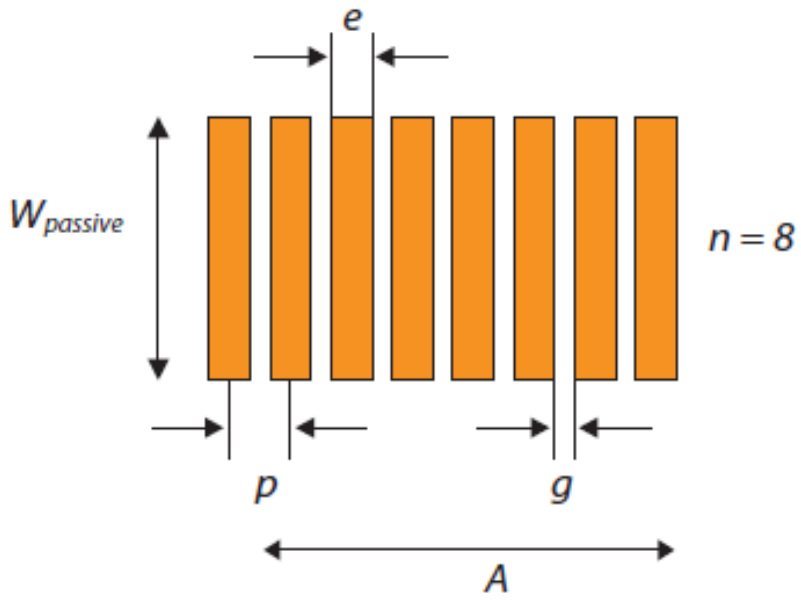

Figure 13: Parameters of a phased array probe [29]

the aperture has to be large.

Another important factor for the beam shape is the passive aperture $W_{passive}$ affecting the beam width and the beam-diffracted pattern (Fig. 15).

3.2.2 Beam Steering and Focusing

In the previous sections it was explained how time delays between the pulsing of individual elements in a phased array probe can be used to generate a steered and focused beam. In this section, beam steering will be briefly mathematically examined by analyzing the far field behavior of an array. A comprehensive derivation of the following equations can be found in [15]. Although both linear and 2-D arrays consist of 2-D elements producing ultrasonic waves propagating in three dimensions, the individual 2-D elements in a probe will be considered as 1-D sources of sound. This simplified model (Fig. 16a) is feasible since the physics of wave propagation is similar for both 1-D and 2-D elements. With the law of cosines we can derive from Fig. 16a)

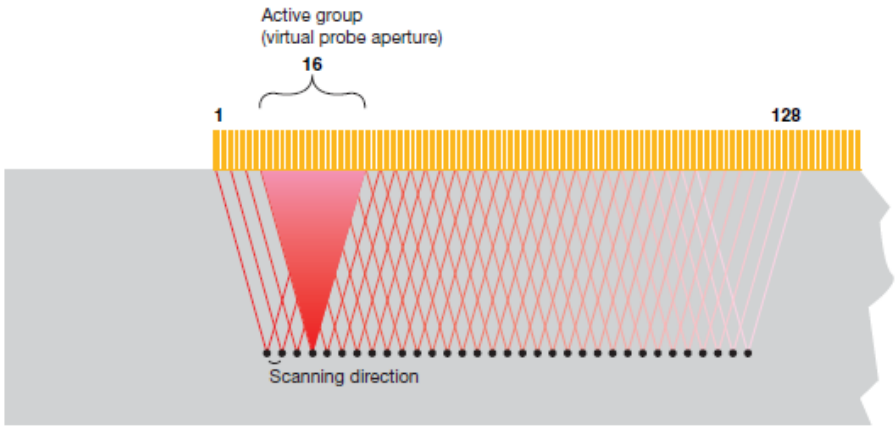

Figure 14: Illustration of the aperture of a phased array probe [29]

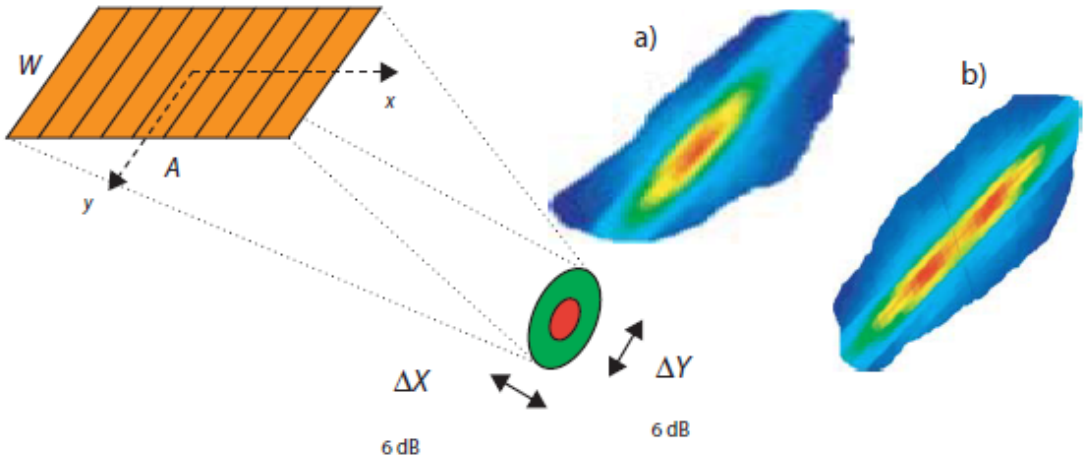

Figure 15: Influence of the passive aperture $W_{passive}$ on the beam shape. The images are received with a 32 element and 5MHz probe, pitch $p = 1$mm and a focus depth of $F = 50$ mm for a) $W = 10$ mm and b) $W = 8$ mm [29].

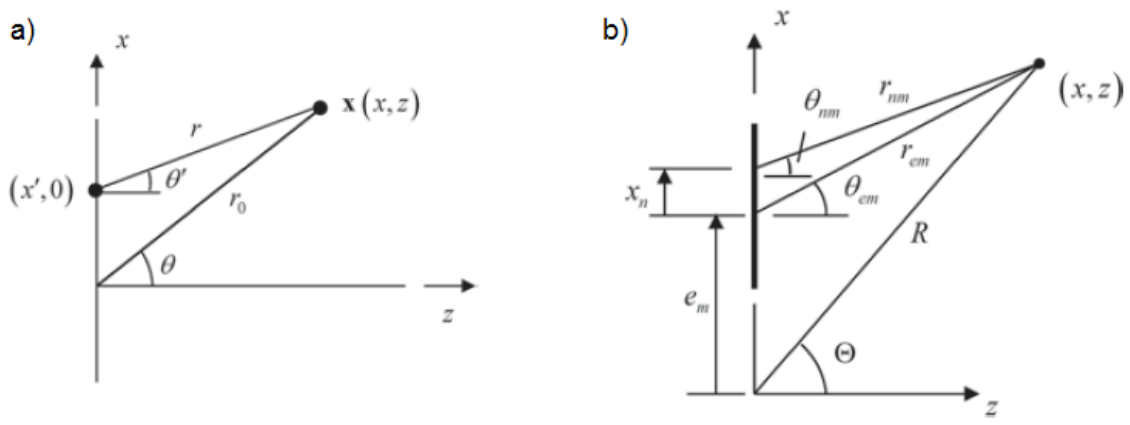

Figure 16: a) Geometry parameters of a 1-D sound source for determining the far field response of a) a single element model and b) an array model [15].

that

$$r = \sqrt{r_0^2 + (x')^2 - 2x' r_0 \sin(\theta)} \tag{50}$$

which can be simplified to

$$r = r_0 - x' \sin(\theta) \tag{51}$$

by using the far field approximation $\frac{x'}{r_0} << 1$. The far field is defined as the region far enough from an element. With this approximation the element response in the far field can be formulated as

$$p(x, w) = \sqrt{\frac{k}{2\pi i}} \rho c V(k_x) \frac{e^{ikr_0}}{\sqrt{r_0}} \tag{52}$$

where $V(k_x)$ describes the spatial Fourier transform of the velocity field

$$V(k_x) = \int_{-b}^{b} v_0(\omega) e^{-ik_x x'} \, \mathrm{d}x' = \frac{2v_0(w)\sin(kb\sin(\theta))}{k\sin(\theta)} \tag{53}$$

In this equation $k = \frac{\omega}{c}$ is the wave number and $k_x = k\sin(\theta)$. However, the motion on the face of an element is being modeled in the sense of a piston element as if the velocity over the entire length of the element is spatially uniform. Therefore,

$$v_z(x', 0, \omega) = \begin{cases} v_0(w) & -b < x' < b \\ 0 & otherwise \end{cases} \tag{54}$$

Then, the response of the piston element in the far field can be written as

$$p(x,\omega) = \rho c v_0(\omega)\sqrt{\frac{2}{\pi i}}(kb)\frac{sin(kb\sin(\theta))}{kb\sin(\theta)}\frac{e^{ikr_0}}{\sqrt{kr_0}} \tag{55}$$

where

$$D_b(\theta) = \frac{\sin(kb\sin(\theta))}{kb\sin(\theta)} \tag{56}$$

is the directivity function of a single element transducer. However, for a phased array probe the entire array can be represented by a single line source (Fig. 16b) where we can use the far field approximation $\theta_{em} \cong \Theta$ to write

$$r_{em} = \sqrt{R^2 + e_m^2 - 2Re_m\sin(\Theta)} \cong R - e_m\sin(\Theta) \tag{57}$$

where e_m is measured from the origin to the m-th element and can be computed as follows:

$$e_m = \left(\frac{2m-1-M}{2}\right)s. \tag{58}$$

Then, the response can be formulated as

$$p(x,w) = \sum_{m=1}^{M}\tilde{C}_m e^{i\omega\Delta t_m}\left[\rho c v_0\sqrt{\frac{2}{\pi i}}kbD_b(\Theta)\frac{e^{ikR}}{\sqrt{kR}}e^{-ike_m\sin(\Theta)}\right] \tag{59}$$

For a time-delay of $\Delta t_m = 0$ and $\tilde{C}_m = 1$ equation (59) can be rewritten by using the solution for a geometric series, $\sum_{m=1}^{M} a^m = \frac{a(1-a^M)}{1-a}$,

$$p(x,w) = \rho c v_0\sqrt{\frac{2}{\pi i}}(kbM)D_b(\Theta)\cdot\frac{\sin[(Mks\sin(\Theta))/2]}{M\sin[(ks\sin(\Theta))/2]}\frac{e^{ikR}}{\sqrt{kR}} \tag{60}$$

where M is the number of elements in an array. Equation (59) points out that in the far field of the array the wave field is cylindrical spreading with a total angular directivity of $D(\Theta) = D_b(\Theta)\cdot D_s(\Theta)$. Here, D_s can be considered as the directivity due to a discrete array of point sources which are separated by the distance s.

$$D_s(\Theta) = \frac{\sin[(Mks\sin(\Theta))/2]}{M\sin[(ks\sin(\Theta))/2]} \tag{61}$$

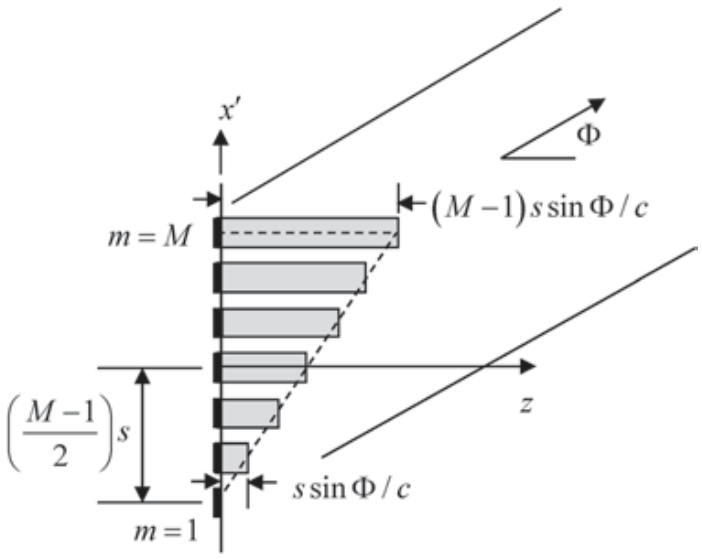

Figure 17: A beam steered to an angle of $\Phi > 0$ due to discrete and linear distributed time delays that are applied to the array

In order to steer a beam (Fig. 17), a time delay of the form

$$\Delta t_m = \begin{cases} \frac{s\sin(\Phi)}{c}(m-1) & \Phi \geq 0 \\ \frac{s|\sin(\Phi)|}{c}(M-m) & \Phi < 0 \end{cases} \tag{62}$$

has to be applied. Then, equation (59) can be formulated as follows

$$\begin{aligned} p(x,\omega) =& \rho c v_0 \sqrt{\frac{2}{\pi i}}(kbM) D_b(\Theta) \frac{e^{ikR}}{\sqrt{kR}} \frac{1}{M} e^{iks(\sin(\Theta)-\sin(\Phi))\frac{M+1}{2}} \\ & \cdot \sum_{m=1}^{M} e^{-iks(\sin(\Theta)-\sin(\Phi))m}, \end{aligned} \tag{63}$$

where $\tilde{C}_m = 1$. Again, by using the solution for a geometric series a directivity function of the form

$$D_s(\Theta,\Phi) = \frac{\sin\left[Mks(\sin(\Theta)-\sin(\Phi))/2\right]}{M\sin\left[ks(\sin(\Theta)-\sin(\Phi))/2\right]} \tag{64}$$

can be obtained. In contrast to steering a beam, time delays of the form

$$\Delta t_m = \frac{s^2}{2R_0 c}(m-1)(M-m). \tag{65}$$

have to be applied in order to focus a beam (Fig. 18).

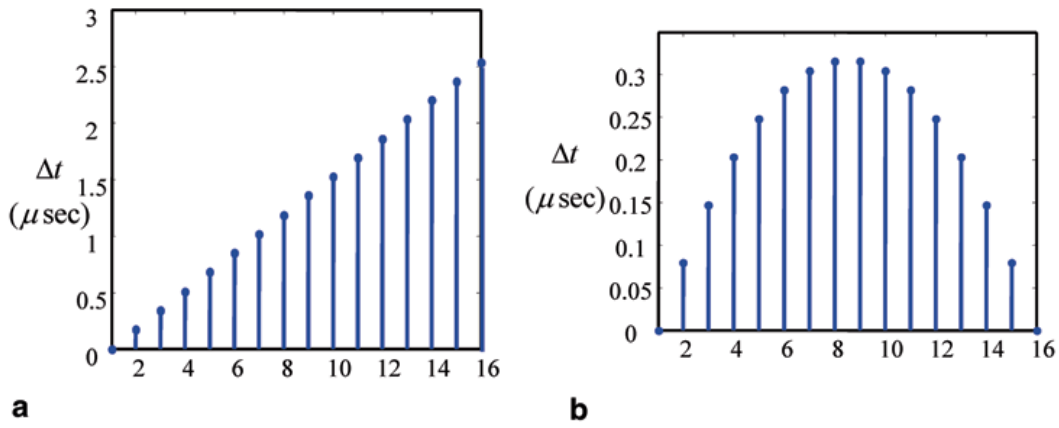

Figure 18: Time delays applied to a 16 element phased array probe to a) steer the beam and b) focus the beam

.

3.3 Phased Array Imaging Methods

Ultrasonic phased array images are basically 2-D projections of the inspected specimen. They are defined by different plane views (top, side and end view) between the scanning parameters and the ultrasonic path (Fig. 19). In the following, A-, B- and S-Scans will be described in detail since they were used in this research. However, in the end of this section the nonlinear imaging method, that was examined in this research, will be introduced.

3.3.1 Linear Imaging

Ultrasonic phased array images are usually generated with the help of two fundamental echo parameters - the echo amplitude A and the place of occurring with respect to the transit time which is correlated to the depth of the reflection s by the following relationship

$$s = v \cdot t \quad , \tag{66}$$

where v describes the velocity of the specimen.

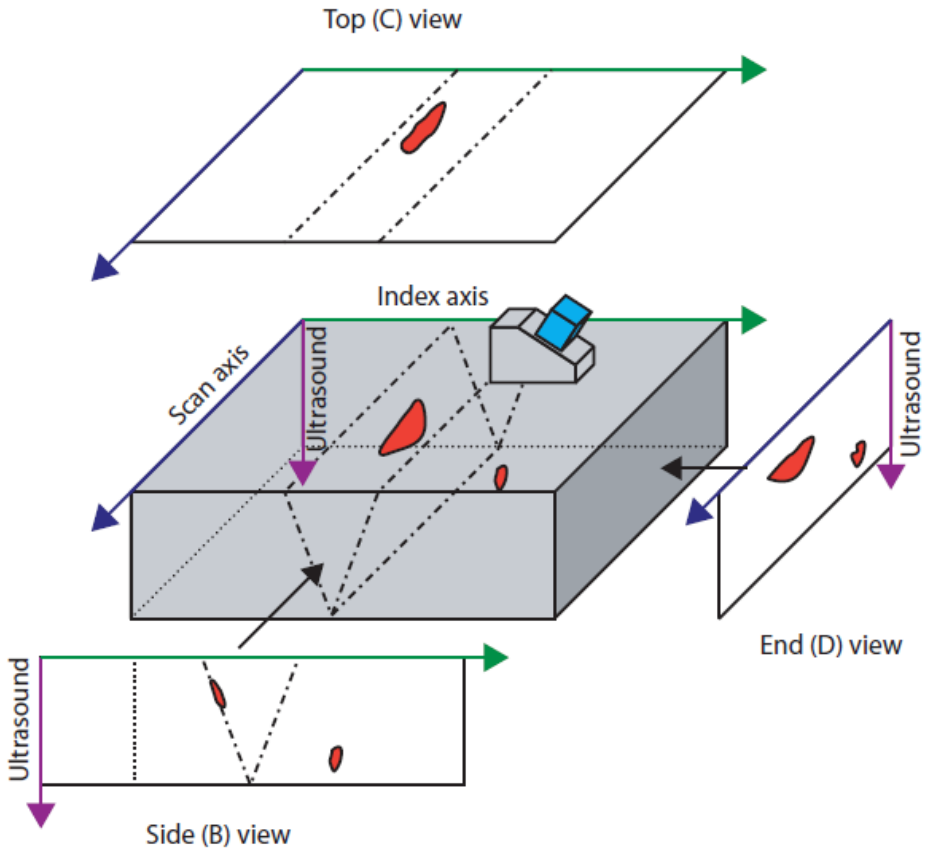

Figure 19: Most common ultrasonic views (Scans) defined by different plane views between the scanning parameters and the ultrasonic path [29].

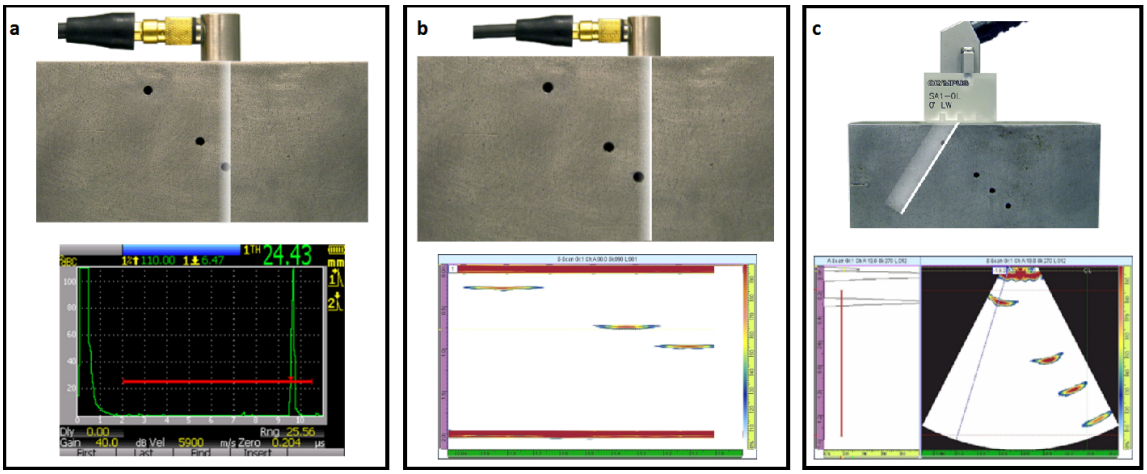

Figure 20: a) A-Scan b) B-Scan c) S-Scan [23]

3.3.1.1 A-, B- and S-Scan

The most basic representation of the received echo amplitude versus the time of flight (ultrasonic path) is an A-scan (Fig. 20a).

Basically, the B-Scan is a 2-D view of recorded A-scan Data where the ultrasound path is plotted over the scan position (Fig. 20b). The stacked A-scan amplitudes are color coded and represented by a time-based sampling position. However, due to beam spread and other factors this kind of scan elongates the defect image and deforms the defect size.

A sectorial scan (S-scan) is a 2-D view of all A-scans recorded for a preset angle range of typically 30° to 70°. The S-scan is corrected for refracted angle and delay. They can be used with longitudinal waves or shear waves and can be contact, immersion or mounted on a wedge. In contrast to the B-scan, an S-scan stacks the received echo amplitudes in polar coordinates such that the vertical axis corresponds to the specimen depth and the horizontal axis to the specimen width. Nevertheless, in order to receive an image, it has to be interpolated between the signals to receive a gradient field of the inspected channel. Looking at the gradient field from above results in an easy analyzable S-scan where vertical cracks occur on a vertical line (Fig. 21).

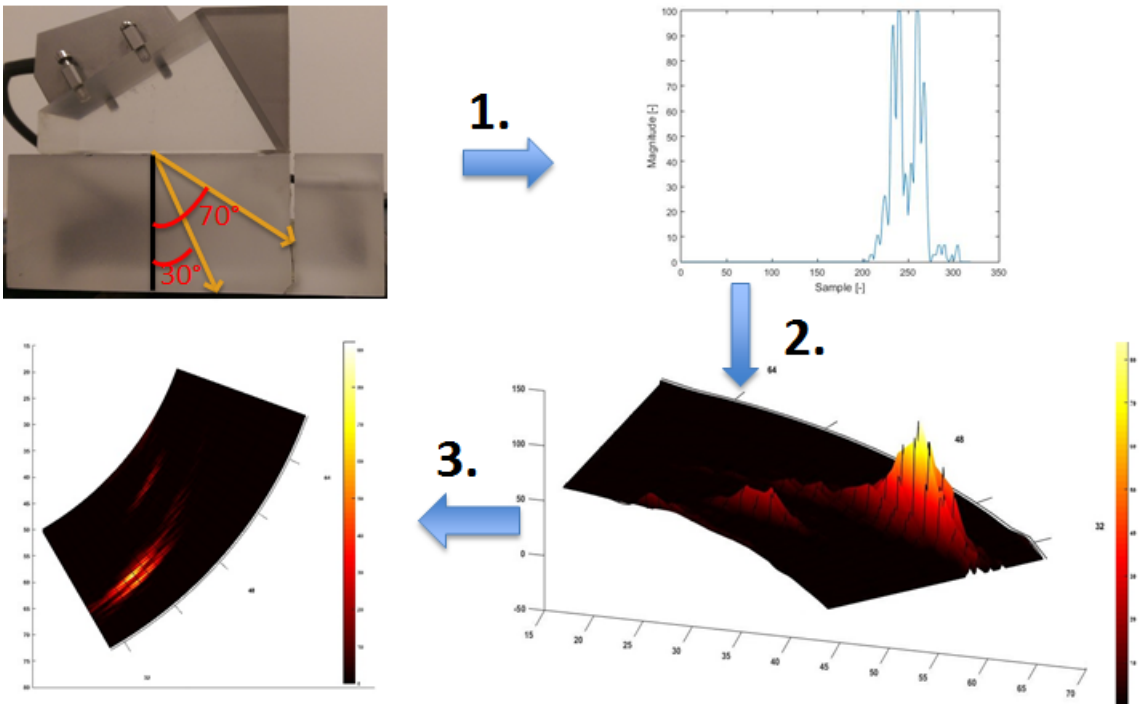

Figure 21: 1.) The response from each angle is digitized. 2.) Stacking the received signals in a polar coordinate system and interpolating between the signals leads to a gradient field. 3.) Looking at the gradient field from above results in an S-scan.

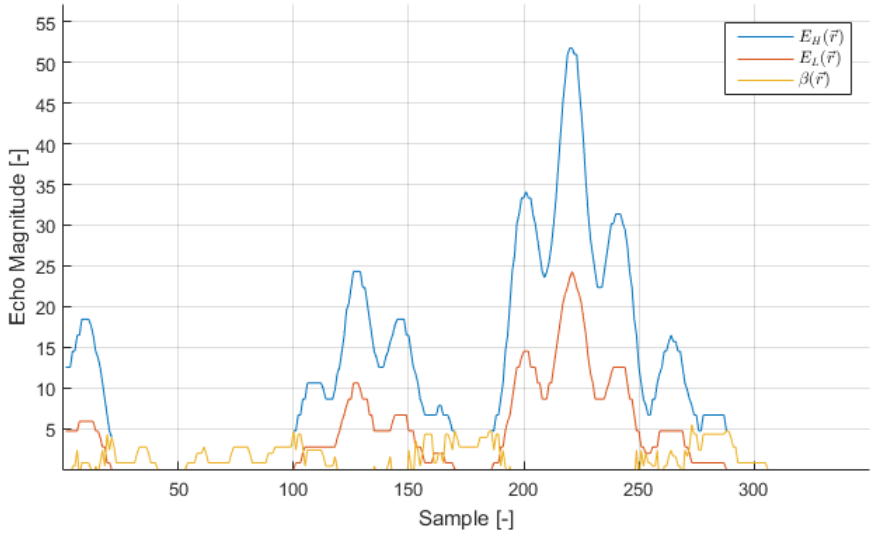

Figure 22: Method of computing the nonlinearity parameter $\beta(\vec{r})$

3.3.2 Imaging the Nonlinearity Metric $\beta(\vec{r})$

The imaging of the nonlinearity metric $\beta(\vec{r})$ is based on the subtraction of signals received at a lower energy level and a higher one (Fig. 22). Consequently, the nonlinearity metric $\beta(\vec{r})$ can be described as follows

$$\beta(\vec{r}) = E_H(\vec{r}) - nE_L(\vec{r}) \quad , \tag{67}$$

where $E_H(\vec{r})$ describes the higher load signals and $E_L(\vec{r})$ the signals received at the lower energy level. Since the commercial phased array system that was used in this research contains two energy loads of 40V and 80V, the input ratio n equates to 2. Again, by stringing together the nonlinear signals for each angle - as described in Fig. 21 - and interpolating between the signals the gradient field for the nonlinear metric of the investigated channel can be received enabling an analysis of the nonlinear crack behavior.

CHAPTER IV

EXPERIMENTAL SET-UP

In the first part of this chapter the experimental set-up will be discussed. In the second part, the adjustment of the ultrasonic parameter including the configuration of the computer based instrument for driving the probes, pulsing and imaging the receiving signal information as well as the configuration of the focal law for steering the beam. The preparation of the specimen will be described in the last part of this chapter.

4.1 Phased Array System

The experimental set-up is schematically illustrated in Fig. 23. With ultrasonic coupling gel the phased array probe is attached to the wedge and similarly the wedge is attached with the specimen. As already mentioned in 3.3.1 the phased array probe is pulsed by the computer-based instrument and the response from each angle is digitized at first, for both the 40V and 80V signals. With a specific software it is possible to transfer the received echo signals from the OmniScan to a computer which can be afterwards used - in a post-processing step with Matlab - to generate the nonlinear image of the inspected channel, corresponding to equation (67) (Fig. 23). Before phased array inspections can be performed on specimens appropriate ultrasonic parameter have to be adjusted in the computer based instrument. In a first step, the dimensions, the material, the geometry of the specimen and whether a weld is present or not have to be specified. The adjustment for the Plexiglas and aluminum specimen can be seen in Table 3.

In the next step, the probe and the wedge have to be specified which are usually automatically identified by the OmniScan (Tab. 4). A phased array probe with 16

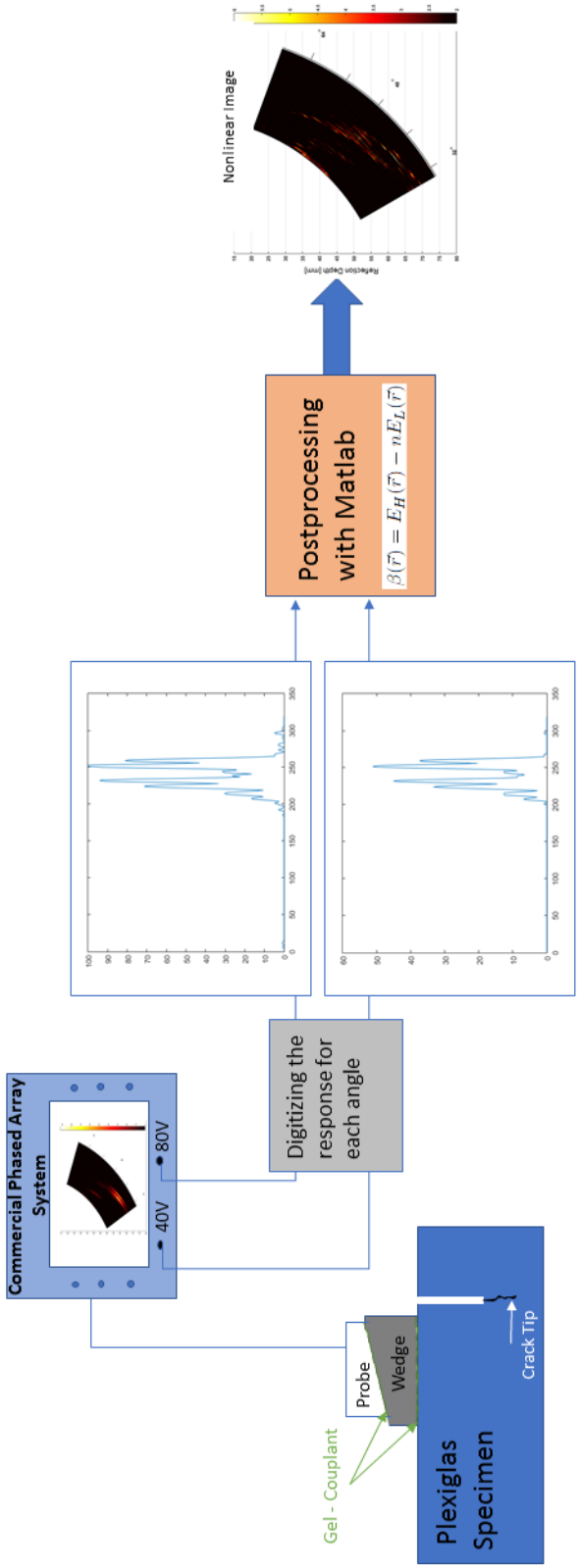

Figure 23: The experimental setup of the phased array inspection including the nonlinear image generation in the postprocessing step.

	Thickness (mm)	Material	Geometry	Weld
Aluminum	15	Aluminum	Plate	None
Plexiglas	47	Plexiglas	Plate	None

Table 3: Adjustment for the Plexiglas and aluminum specimen

Probe	Wedge
1.5L16 - A4	SA4 - N45S

Table 4: Setting for the Probe and the Wedge

elements and a frequency of 1.5MHz was used as well as a SA4 - N45S wedge which means that this wedge leads to a refracted angle of 45° in steel.

After that the focal law configuration and the wave type have to be adjusted. In the focal law configuration, a sectorial, linear or linear at 0° can be selected. In the following, the differences between these three inspection methods will be explained briefly.

- Sectorial: Provides a multiple-angle scan.
- Linear: Provides a linear scan at a configurable angle.
- Linear at 0°: Provides a volume-corrected linear sweep at zero degrees.

Also, inspections using longitudinal waves (LW) or shear waves (SW) can be selected. Furthermore, the number of elements in the aperture have to be adjusted. The set-up for this part can be seen in Tab. 5. Finally, the beam configuration has to be set-up

	Law Configuration	Wave Type	Element Quantity
Aluminum Specimen	Sectorial	LW	6
Plexiglas Specimen	Sectorial	LW	8

Table 5: Settings for the law configuration, the wave type and the used aperture for both the aluminum specimen and the Plexiglas one.

	Min. Angle [°]	Max. Angle [°]	Angle Step [°]	Focus Depth [mm]
Aluminum Specimen	40	80	1	50
Plexiglas Specimen	30	70	1	45

Table 6: Beam configuration for both the aluminum and Plexiglas specimen.

which is done in the *focal law*. Here, the inspection channel can be selected by setting up the minimum and maximum angle of the ultrasonic waves as well as the angle step and the focus depth of the beam. The setting for the beam configuration can be seen in Tab. 6.

4.2 Transducer

The main elements of phased array transducers are usually thin plates of piezoelectric material that convert electronic energy in mechanical energy in form of ultrasonic waves. When a flaw occurs in the specimen the waves will be reflected and the impulse of the reflection can be converted into electronic signals by the piezoelectric material. Afterwards, the magnitude of the echo signal can be computed by the following relation between the initial signal E_i and the echo signal E_e:

$$\frac{E_e}{E_i} \cdot 100 \quad [\%] \tag{68}$$

Having said this, the magnitude of the echo signal corresponds to the size of the material flaw. With this relation, the spot in the material with the biggest defect is easily illustratable (Fig. 24).

As already mentioned in the previous chapter a phased array probe with 16 elements and a frequency of 1.5MHz was used (Fig. 25). However, in Tab. 7 and 8 the dimensions and further specifications of the phased array probe is specified.

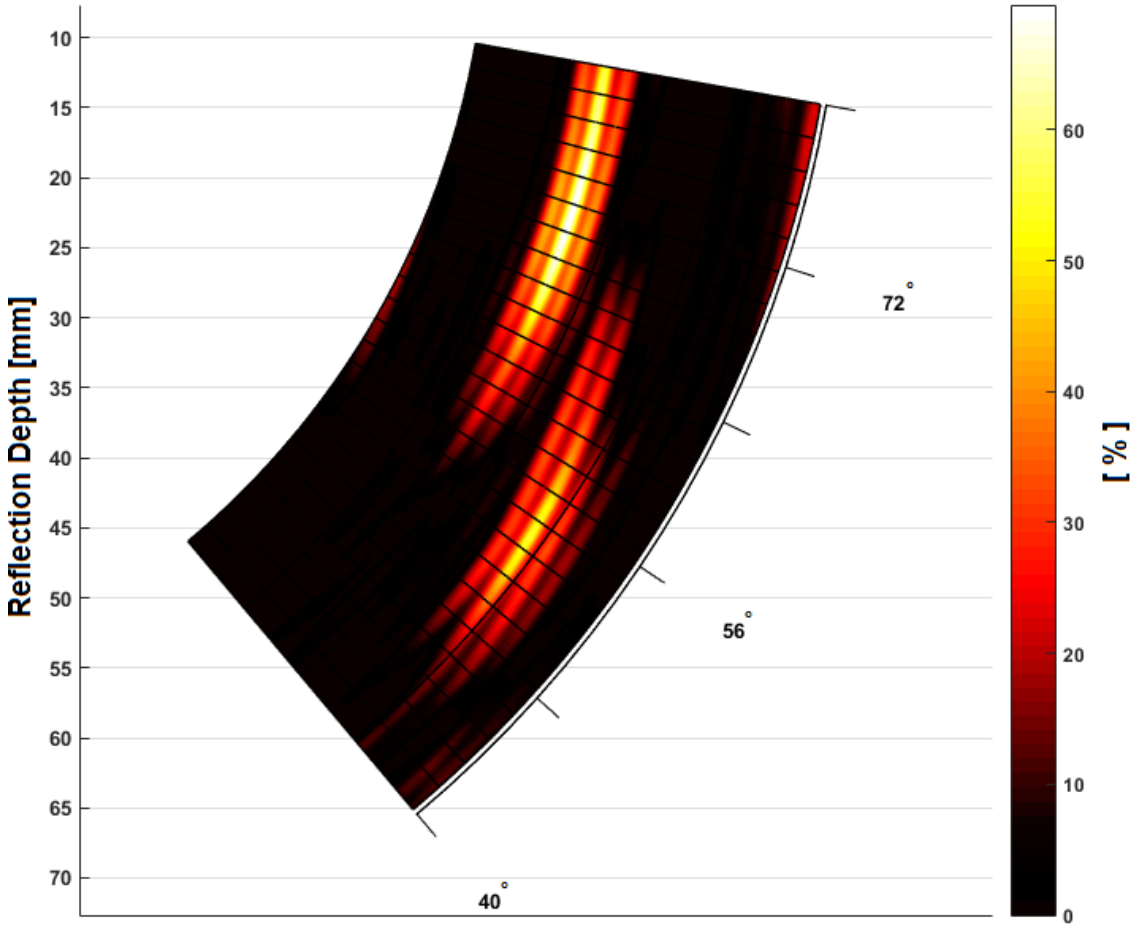

Figure 24: Inspection of a CT aluminum specimen of 15mm thickness. The color scale corresponds to the intensity of the reflected echo signal and therefore to the spot with the biggest material defect in the specimen.

	Frequency [MHz]	Number of elements	Pitch [mm]	Active aperture [mm]
1.5L16 - A4	1.5	16	2.80	44.8

Table 7: Probe specification

	Probe Dimensions [mm]		
	L	W	H
1.5L16 - A4	57	46	30

Table 8: External probe dimensions

Figure 25: Ultrasonic phased array probe with a frequency of 1.5 MHz and 16 elements

	Wedge Dimensions [mm]		
	L	W	H
SA4 - N45S	90	47	51

Table 9: Wedge dimensions

4.3 Wedge

The wedge that was used in this research consists of a high performance plastic called Rexolite (Fig. 26). These wedges - in combination with an impedance matched acoustic absorber for minimizing internal reflections within the wedge - incorporate a pyramidal scattering surface. Such Rexolite wedges have the advantage of reducing internally scattered noise in contrast to conventional wedges. The dimensions of the wedge can be seen in Tab. 9.

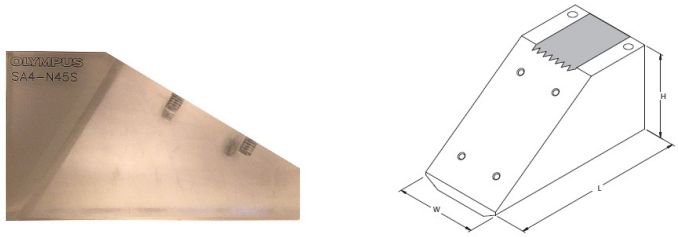

Figure 26: Wedge for a angle beam probe

4.4 Specimen

In this section the preparation of the aluminum and the Plexiglas specimen as well as the developement of the crack will be discussed. To begin with, the dimensions of the specimen will be illustrated in the following. A CT aluminum specimen was used with a thickness of 15 mm and a notch length of 40 mm (Fig. 27 a)). For the carried out experiments the initial notch width of $d_1 = 3.8mm$ was stretched in 2 mm steps until a final width of $d_1 = 4.4mm$ was reached. For the Plexiglas experiments a squarish block with a side length of 50 mm and a width of 132 mm was prepared (Fig. 27 b). Here, the characteristic measure for the carried out experiments is again the initial notch width, in this case $d_2 = 2mm$. Since Plexiglas is brittle and thus more sensitive to a stress intensification than aluminum - especially in the region around the notch tip - the stretching of the Plexiglas notch was performed in 0.25 mm steps until a notch width of $d_2 = 2.5mm$ was reached. However, for both the aluminum and Plexiglas specimen the force for stretching the notch was applied mechanically. In order to stretch the notch of the aluminum specimen, two rods were used, each with a length of 50 cm, connected at the top and at the bottom through threaded bars and nuts (Fig. 28a). Then, the nuts were screwed in the outer direction in order to push the rods apart and consequently create a force on the notch that leads to a stretching of the crack. Slightly different the notch of the Plexiglas specimen was stretched. Here, two screws that were screwed in from the side wall of the specimen were used to push apart the left and right side of the notch (Fig. 28 b).

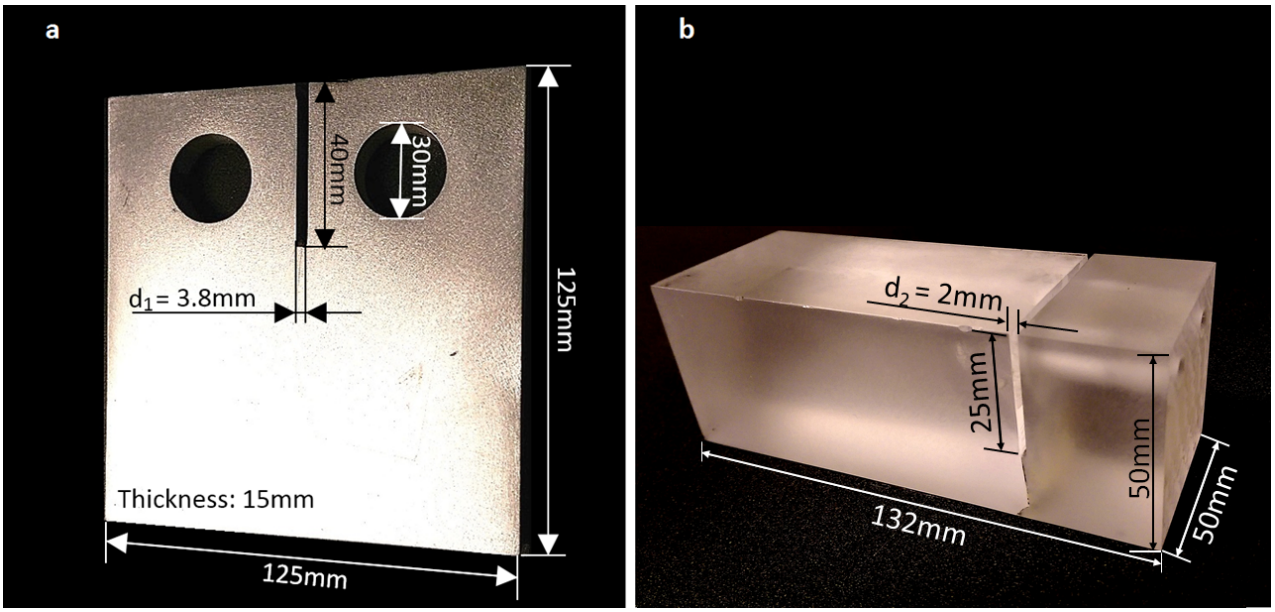

Figure 27: Dimensions of a) the aluminum specimen and b) the plexiglas one.

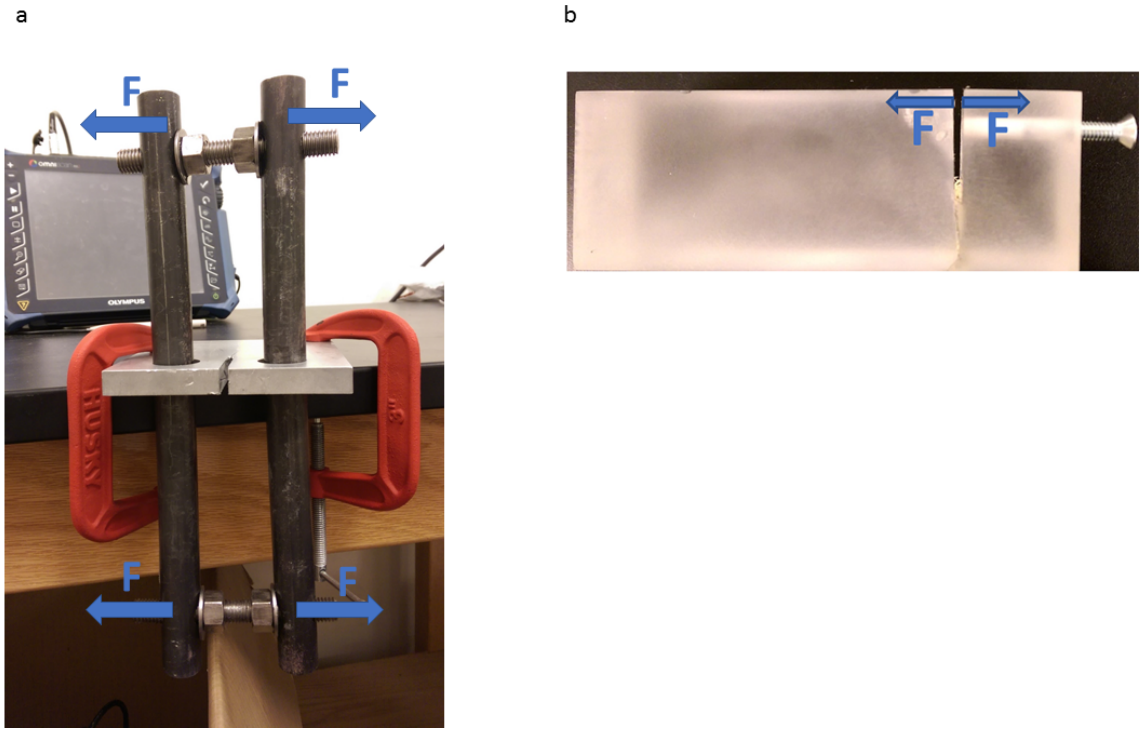

Figure 28: a) Stretching the crack in the aluminum specimen through a mechanically applied force on the rods by screwing the nuts in the outer direction. b) Stretching the crack in the Plexiglas specimen through a mechanically applied force on the notch by screwing in two screws from the side wall.

CHAPTER V

RESULTS AND INTERPRETATION

The results of the ultrasonic phased array measurements performed on the aluminum and Plexiglas specimen will be discussed in the following. The main purpose for investigating the nonlinear imaging method - by using the nonlinearity metric $\beta(\vec{r})$ - was to identify the true depth of a fatigue crack. In this sense, the results for the Plexiglas specimen clearly demonstrate the efficiency of the proposed imaging method of nonlinear defects. However, for the aluminum specimen the results could not lead to a promising demonstration of this method even though the crack tip could be determined. This can be explained by the fact that in contrast to the Plexiglas specimen, where the crack grows in the vertical direction relative to the phased array probe, the crack in the aluminum specimen grows in the horizontal direction for which reason an identification of the real crack depth is not even possible.

5.1 Aluminum Specimen

Before the results are going to be explained in the following the determination of the crack in the linear image have to be explained briefly. Since the phased array probe lies perpendicular to the direction of the crack growth the linear images will illustrate two main characteristics which are the upper and the lower side of the crack (Fig. 30a and 30b). In this image, the strongest echo signal appears at a reflection depth of $30mm$ and $45mm$. At this point it is important to note that for both the aluminum and Plexiglas specimen the "Reflection Depth" - as the vertical axes were labeled in the images - does not equate to the true depth of the crack within the specimen! It rather describes the traveled distance of the beam until it was reflected back by a defect, for instance. However, taking the difference of both depths yields a length of

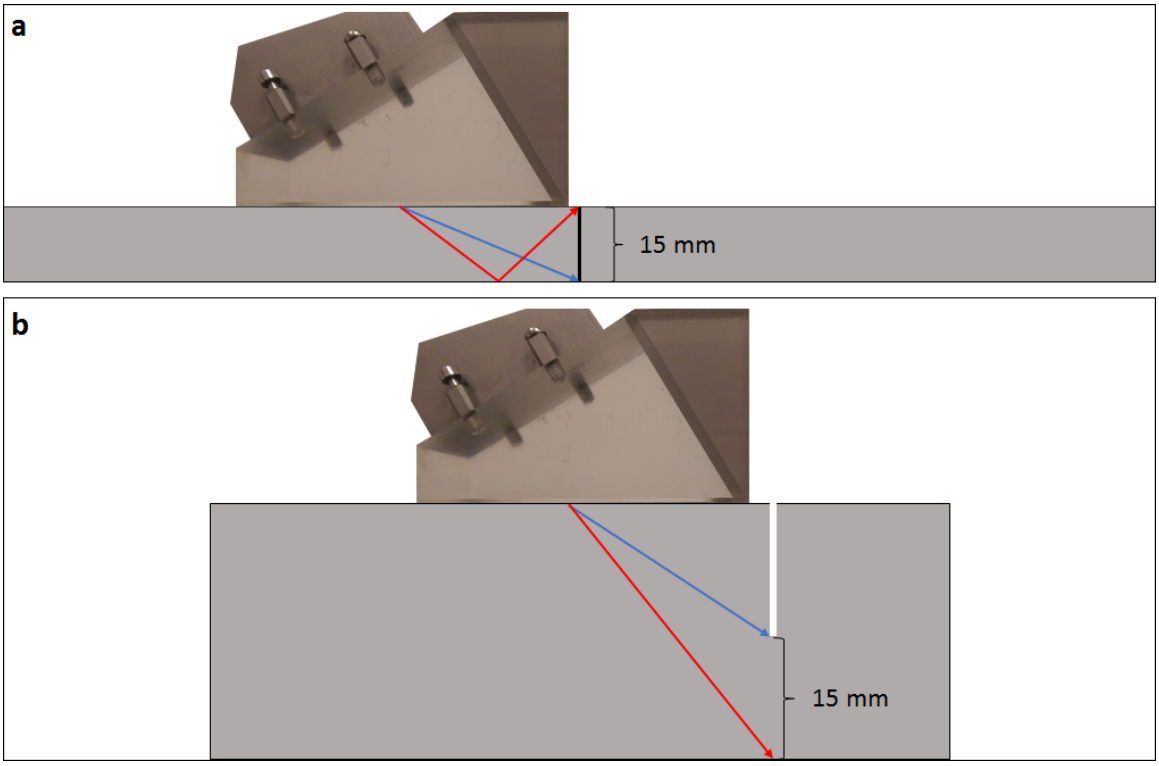

Figure 29: Schematic illustration of how the crack was detected in a) the aluminum and b) the Plexiglas specimen.

$15mm$ corresponding to the thickness of the specimen. Calculations like that have to be done in order to have an evidence that indeed the desired crack is being imaged instead of other potential flaws within the material. In Fig. 29 a) the detection of the particular crack sides is exemplified. Here, the aluminum specimen is presented in a sectional view where the black vertical line of $15mm$ length illustrates the crack. The lower crack side is detected by the beam traveling through the material along the blue arrow whereas the upper crack side is being detected by the beam traveling along the longer, red arrow. Therefore, the detection of the upper crack side appears in the linear image below the detection of the lower crack side.

By looking at Fig. 30 a) and b) no significant difference between the images can be noticed. This is due to the fact that for both the 40V and the 80V image the same color map was used. Before the results will be presented in the following, a last significance in the nonlinear images has to be described. In contrast to the linear

images the color scale in the nonlinear images does not start from 0 which is an approach to reduce the noise in the images as much as possible.

To begin with, measurements were performed on the specimen with closed crack(Fig. 30). As expected, the detection of the upper and the lower crack side disappear in the nonlinear image, since the imaging of the nonlinearity metric $\beta(\vec{r})$ is not dependent on linear scattering. Even though the color scale was adjusted to reduce noise in the image it is still pretty difficult to distinguish between the crack tip and noise. However, by observing the trend of the crack in the linear images it seems reasonable to expect that the crack tip - which is not being imaged in those images, since the beam passes through the crack tip due to the fact that the structural changes within the material are too small around this area for a detection - will connect the upper and the lower crack side. Regarding that, a first indication of the crack tip can be seen in Fig. 30c).

Compared to the linear images of the closed crack there is a noteworthy difference in the linear images for a stretched notch width of $d_1 = 4mm$ indicated with a blue circle in Fig. 32 a). In contrast to the previous images, which seem to have an interruption in the detection of the lower crack side, the images for $d_1 = 4mm$ illustrate a continuous trend of the crack. This can be explained by the fact that due to a small area where the left and right side of the crack perfectly match, the beam will pass through the crack leading to an interruption in the trend of the crack in the linear images (Fig. 31a). By increasing the notch width, this area will be stretched apart such that no waves can pass through the crack anymore resulting in a smooth trend of the crack which can be observed in the linear image (Fig. 31b).

A very distinctive characteristic of the nonlinear image for $d_1 = 4mm$ is especially the fact that the shape of the crack detection appears much sharper. However, compared to result for $d_1 = 3.8mm$ no significant improvement in the detection of the crack tip can be observed.

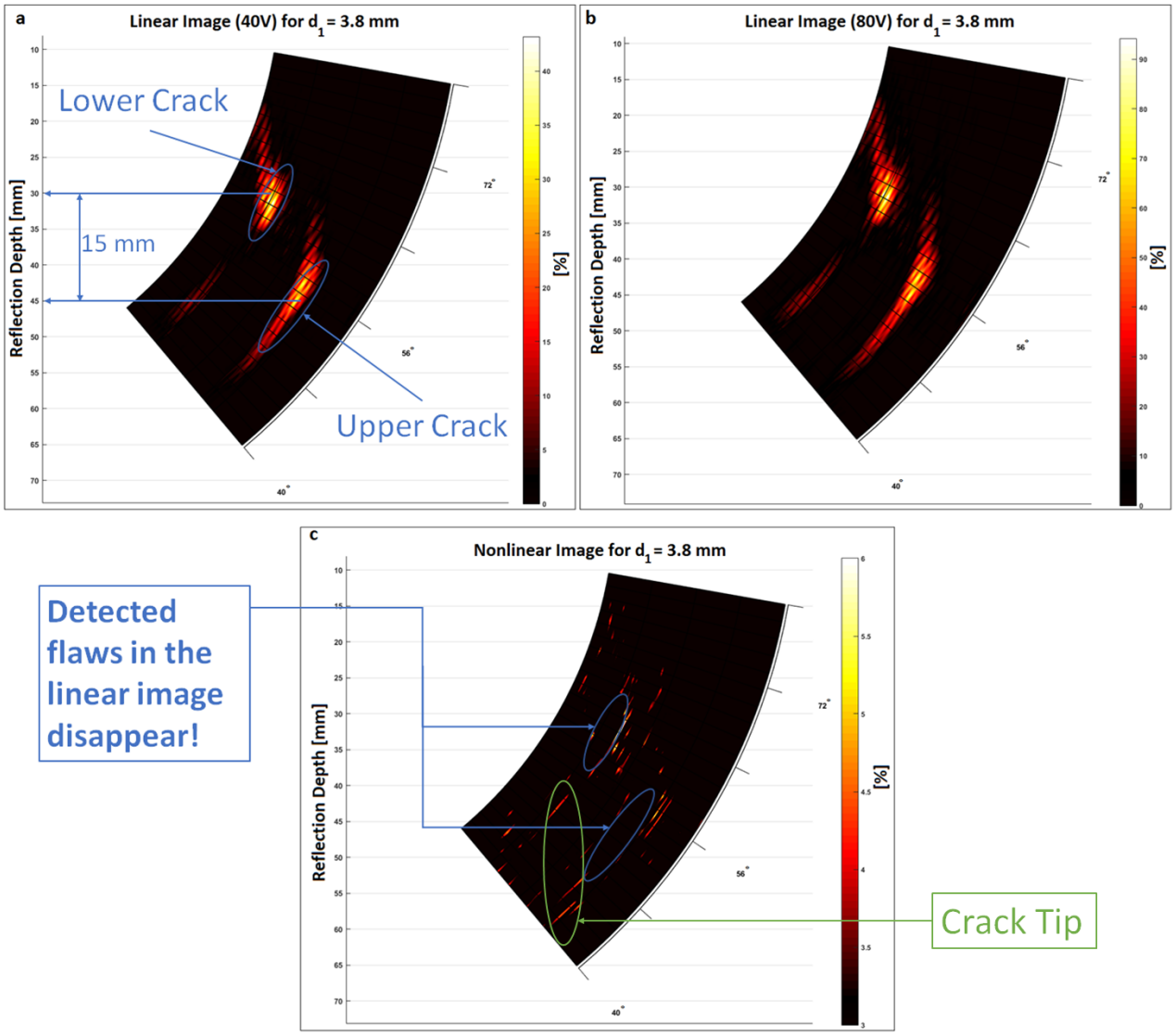

Figure 30: Linear Image of the aluminum specimen for $d_1 = 3.8mm$ (closed crack) with a energy load of a) 40V and b) 80V. c) Image of the nonlinearity metric $\beta(\vec{r})$ for $d_1 = 3.8mm$

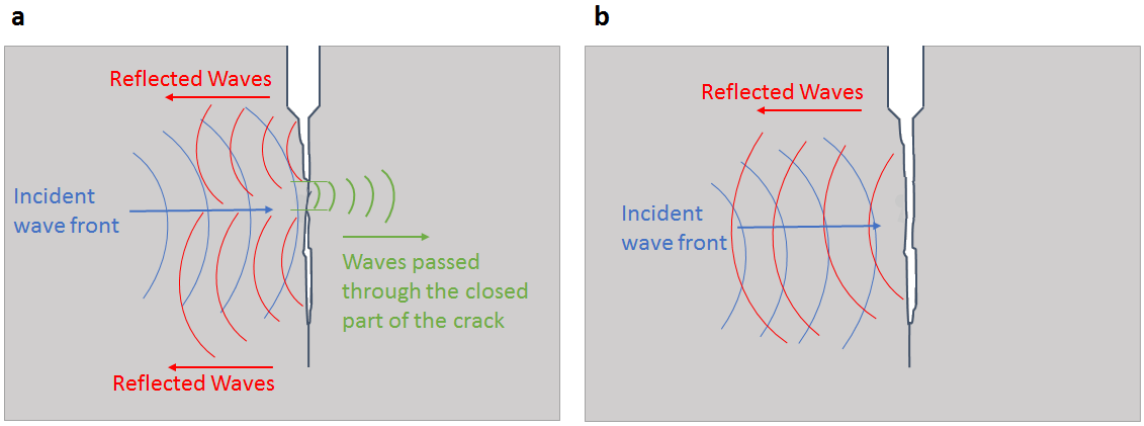

Figure 31: a) In a small area both sides of the crack perfectly match such that the ultrasonic waves pass through leading to an interruption in the trend of the crack in the linear images whereas in b) the crack is completely open such that the whole wave is reflected and a continuous trend of the crack can be seen in the linear images.

Looking at the results for $d_1 = 4.2mm$ and $d_1 = 4.4mm$ the expected connection from the lower crack side to the upper crack side in the nonlinear image, indicating the crack tip, becomes clearer. Evidence for the presence of the crack tip in the nonlinear image can be provided by a small calculation, as already mentioned in the beginning of this section. The difference of the reflection depth for the marked crack tip in Fig. 33 c), which starts at $45mm$ and ends at $60mm$, exactly equates to $15mm$ corresponding to the thickness of the specimen and therefore to the crack tip. Fig. 34 c) can be used as a further indication for the detection of the crack tip since by stretching the notch further apart to a final width of $d_1 = 4.4mm$ a stronger detection can be observed in the green marking, compared to the nonlinear image for $d_1 = 4.2mm$.

Before the results of the Plexiglas specimen will be discussed in the following, a short conclusion about the results for the aluminum specimen should be drawn at this point. The results demonstrate that when d_1 is small the crack tip is not visible in the nonlinear images since the crack is too tight. By increasing d_1 the crack becomes less tight such that the crack tip can be observed in the nonlinear images.

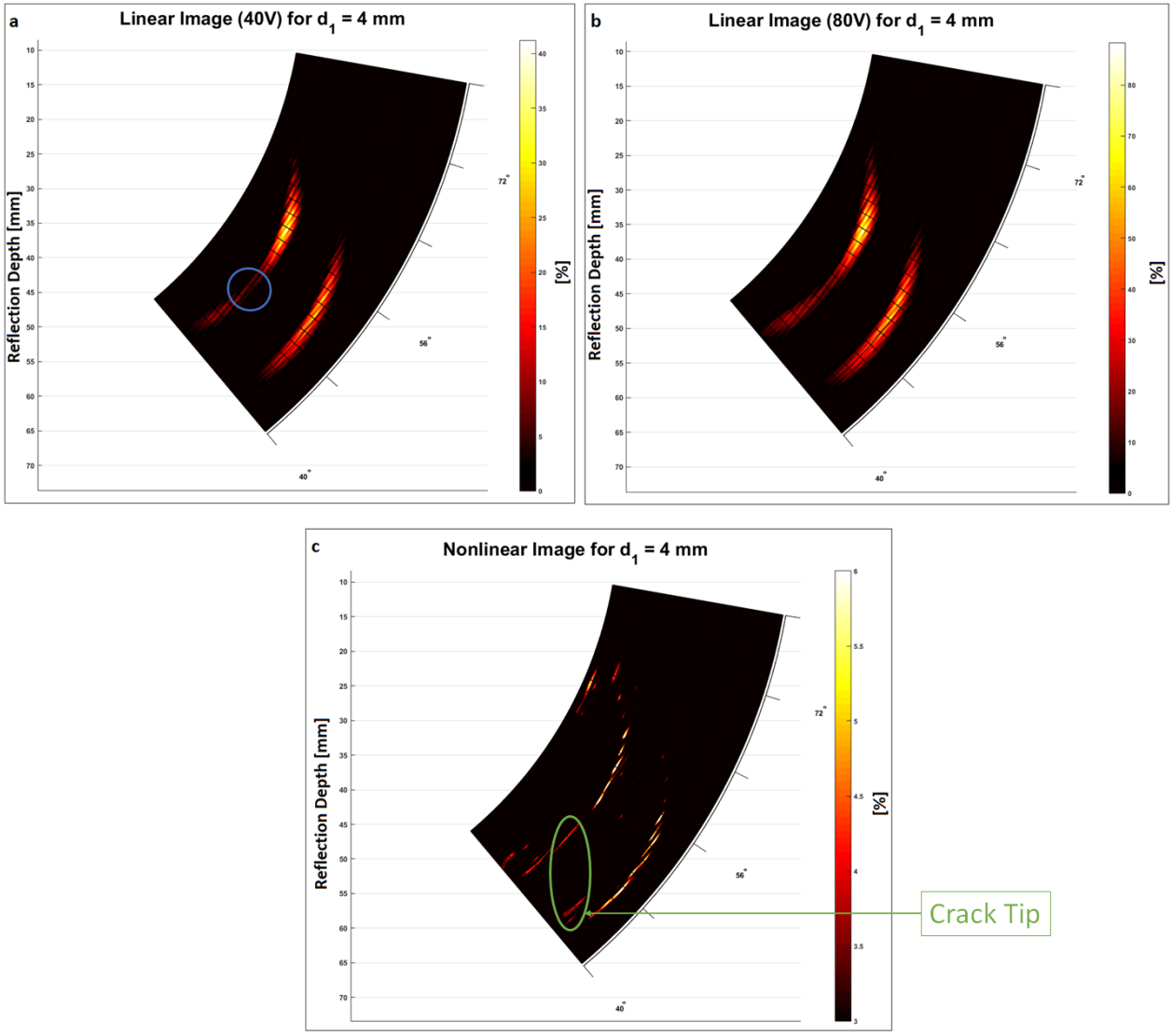

Figure 32: Linear Image of the aluminum specimen for $d_1 = 4mm$ with a energy load of a) 40V and b) 80V. c) Image of the nonlinearity metric $\beta(\vec{r})$ for $d_1 = 4mm$

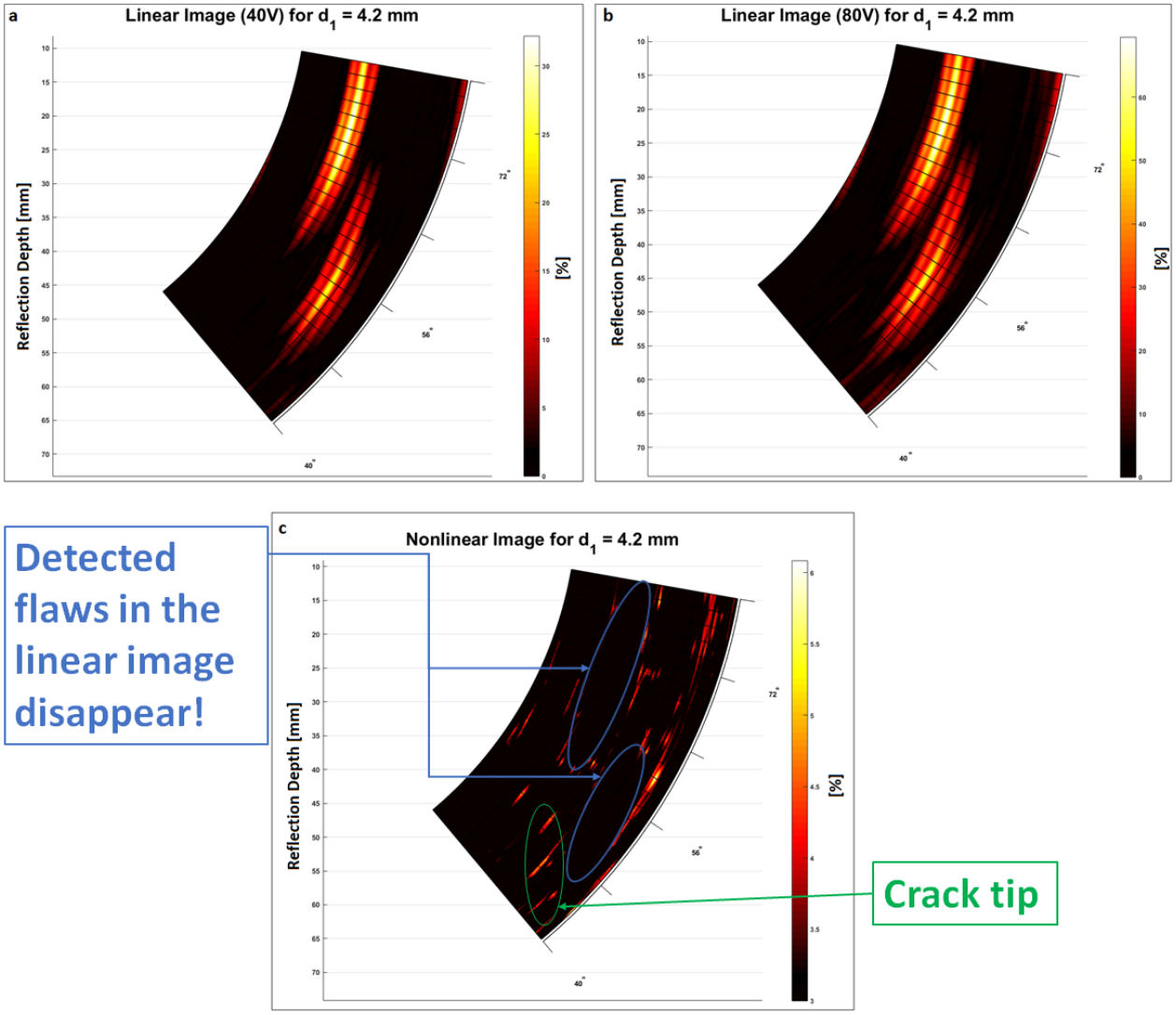

Figure 33: Linear Image of the aluminum specimen for $d_1 = 4.2mm$ with a energy load of a) 40V and b) 80V. c) Image of the nonlinearity metric $\beta(\vec{r})$ for $d_1 = 4.2mm$

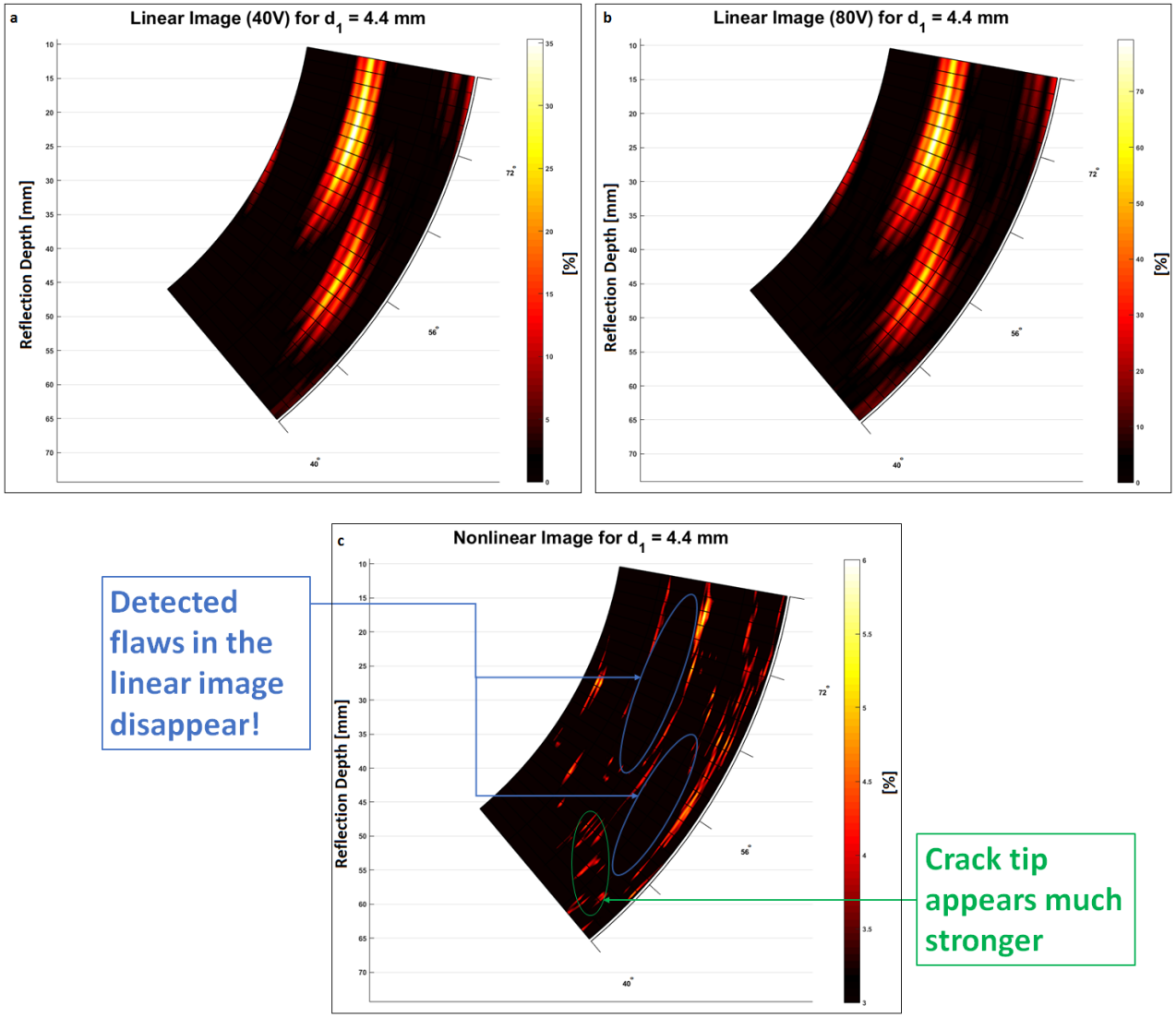

Figure 34: Linear Image of the aluminum specimen for $d_1 = 4.4mm$ with a energy load of a) 40V and b) 80V. c) Image of the nonlinearity metric $\beta(\vec{r})$ for $d_1 = 4.4mm$

5.2 Plexiglas Specimen

In analogy to the previous section, the determination of the crack in the linear image will be discussed at first before the results are going to be presented and analyzed. The Plexiglas specimen was prepared such that the crack grows in the vertical direction relative to the phased array probe. In this way, the true depth of the crack could be investigated. Since the notch tip - and in particular the crack tip - offers a small contact surface, the detection of this area has to appear in the linear images relatively small compared to the reflection of the ultrasonic beam by the bottom of the specimen. With this in mind, the small and comparatively weak detection in Fig. 35a) corresponds to the notch tip whereas the lower detection in this image corresponds to a stronger reflected beam through the back wall. Therefore, a reflection depth of $45mm$ matches up with the blue arrow in Fig. 29b), for the detection of the notch tip, where in contrast to that the red arrow correlates with the back wall reflection right under the notch, with a depth of $60mm$. The reason for desiring to detect the notch tip and the bottom is due to the fact that by stretching the notch the crack will expectedly grow in the vertical direction to the bottom of the specimen which should also be visible in the nonlinear images as a vertical connection between the notch tip and the back wall reflection. However, the difference of $15mm$ corresponding to the distance between the notch and the bottom is a first indication for the right detection. Practically, the back wall reflection in the linear image was verified by a simple method. By putting coupling gel at the finger tip and spreading it over the bottom of the specimen a change in the detection and in particular the finger movement itself could be observed.

By comparing the linear images with the nonlinear one in Fig. 35 it is noticeable that the reflections of the notch and the back wall disappear in the nonlinear image, as expected. Since the notch is not stretched at all in the first investigation of the specimen, it seems reasonable that in Fig. 35c) no reflections between the notch and

the bottom, and therefore no crack growth, can be detected.

In the second measurement the notch was stretched to a width of $d_2 = 2.25mm$. Nevertheless, no detection of a crack growth can be seen in the linear images of Fig. 36. In contrast to that, a crack growth in the vertical direction, initiated by the notch tip, can be recognized in the nonlinear image. By calculating the difference between the reflection depth of the notch tip and the crack tip - which is marked green in Fig. 36c) - the depth of the crack can be determined. In this case, a crack of $\sim 4mm$ length, right below the notch tip, has developed.

In the third measurement the notch was stretched further apart to a final width of $d_2 = 2.5mm$ and still no detection of the crack growth can be observed in the linear images of Fig. 37. On the contrary to the linear images, the nonlinear one clearly shows a trend of the crack growing from the initiation at the notch tip to the bottom of the specimen. For this case, a crack tip that appears $\sim 10mm$ below the notch tip can be observed. Having said this, by stretching the notch to a width of $d_2 = 2.5mm$ a depth of $\sim 35mm$ for the crack tip, below the surface of the specimen, can be determined.

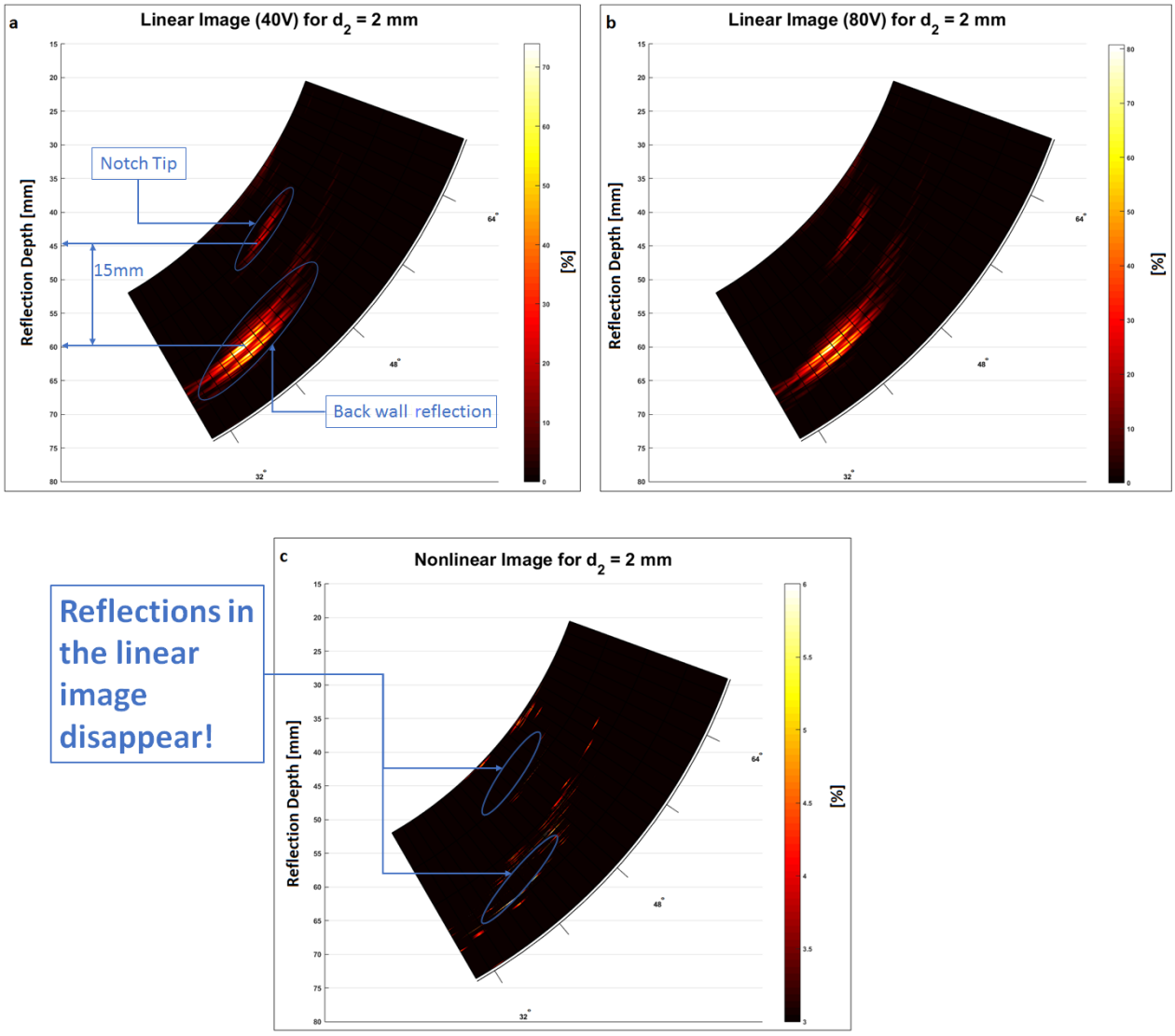

Figure 35: Linear Image of the Plexiglas specimen for $d_1 = 2mm$ with a energy load of a) 40V and b) 80V. c) Image of the nonlinearity metric $\beta(\vec{r})$ for $d_2 = 2mm$

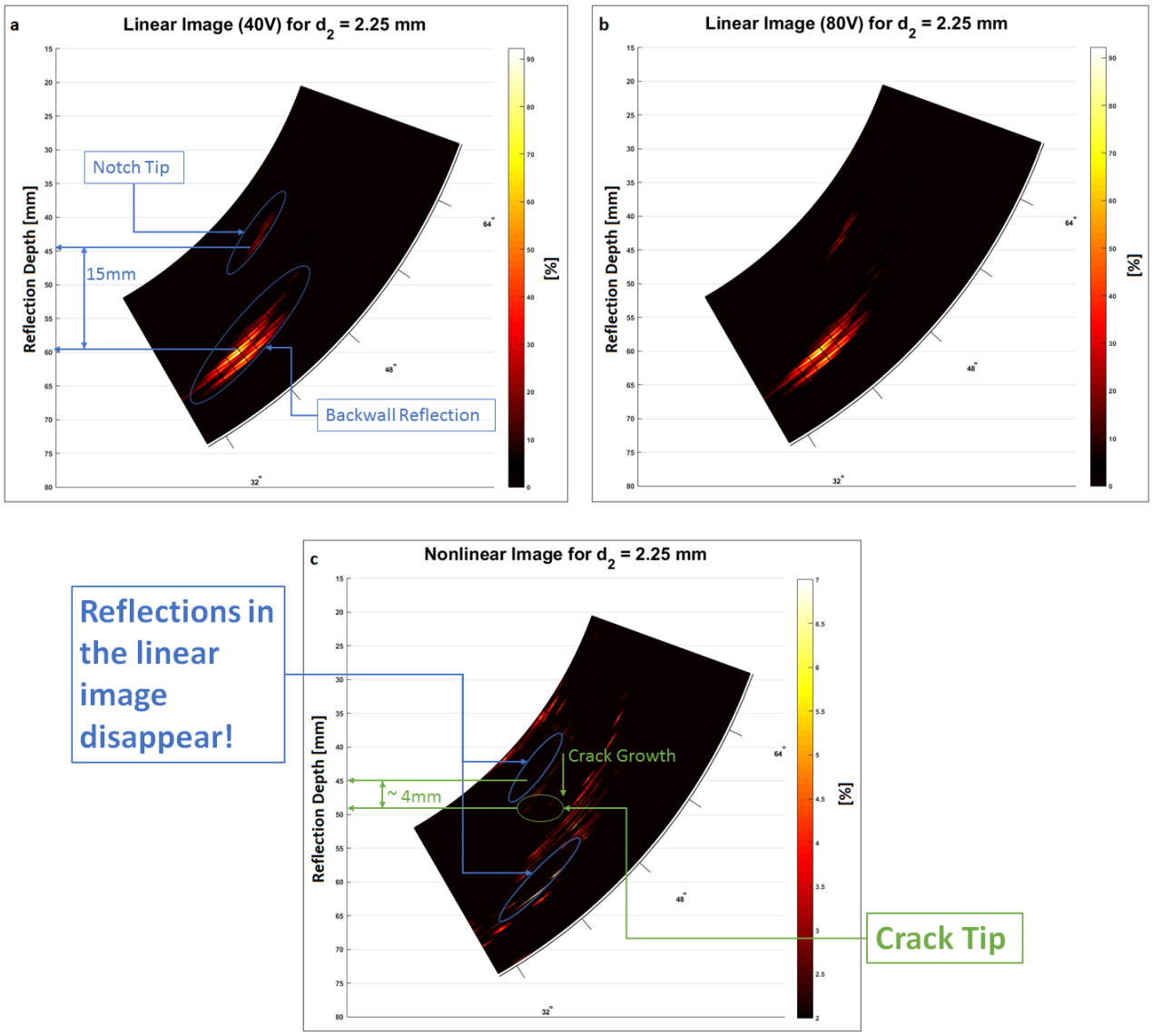

Figure 36: Linear Image of the Plexiglas specimen for $d_1 = 2.25mm$ with a energy load of a) 40V and b) 80V. c) Image of the nonlinearity metric $\beta(\vec{r})$ for $d_2 = 2.25mm$

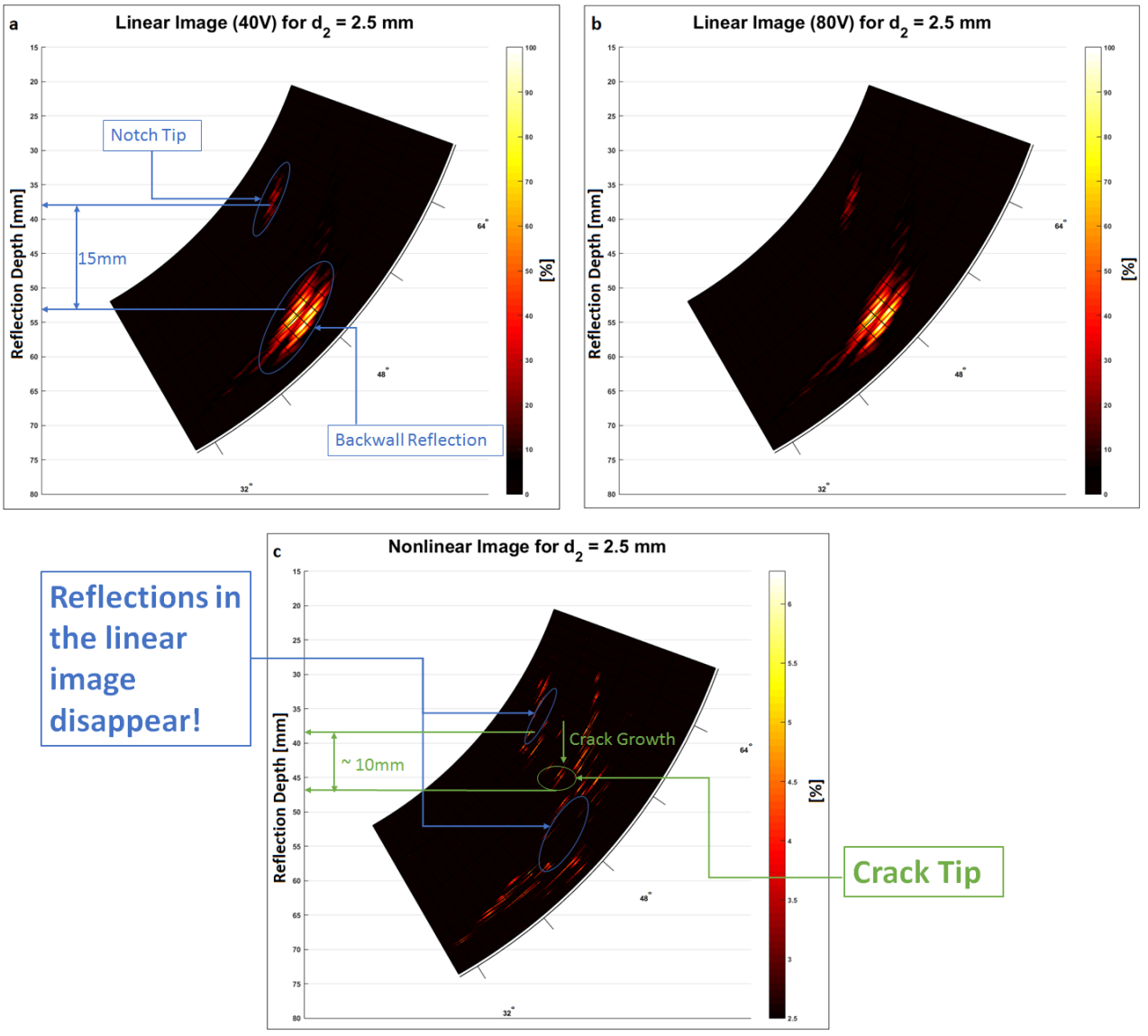

Figure 37: Linear Image of the Plexiglas specimen for $d_1 = 2.5mm$ with a energy load of a) 40V and b) 80V. c) Image of the nonlinearity metric $\beta(\vec{r})$ for $d_2 = 2.5mm$

CHAPTER VI

CONCLUSION AND OUTLOOK

Since linear imaging methods are limited in the capability of monitoring challenging (nonlinear) defects within materials, such as small fatigue cracks in the early stages, partially- and fully- closed cracks, the aim of this research was to obtain images of such parts of a crack using a nonlinear ultrasonic phased array method. This research presents a nonlinear imaging method based on the nonlinearity metric $\beta(\vec{r})$ that subtracts signals received at a lower energy level and a higher one. It is important to note that for the performed experiments a *commercial* phased array system, with a limited energy load choice of 40V and 80V, was used. The measurements were performed on both an aluminum specimen and a Plexiglas one. The main advantage of the Plexiglas specimen over the aluminum one is the fact that the initiated crack grows in a vertical direction such that the efficiency of the purposed imaging method can be demonstrated by determining the depth of the crack. In this connection, a first measurement was performed with an unstressed notch in which naturally no crack growth was detected in the nonlinear image. However, by stretching the notch to a width of $d_2 = 2.25mm$ and $d_2 = 2.5mm$ an increasing crack growth could be observed in the nonlinear images. Instead of trying to detect the depth of a crack - as it was done with the Plexiglas specimen - the main purpose of the performed experiments with the aluminum one was to identify and to detect the crack tip which is not possible with linear imaging methods, since the structural changes within the material around the crack tip are way too small in order to be detected by an ultrasonic beam. However, using the presented imaging method of the nonlinearity metric $\beta(\vec{r})$ it was demonstrated that the crack tip can be detected. In fact, for a completely closed

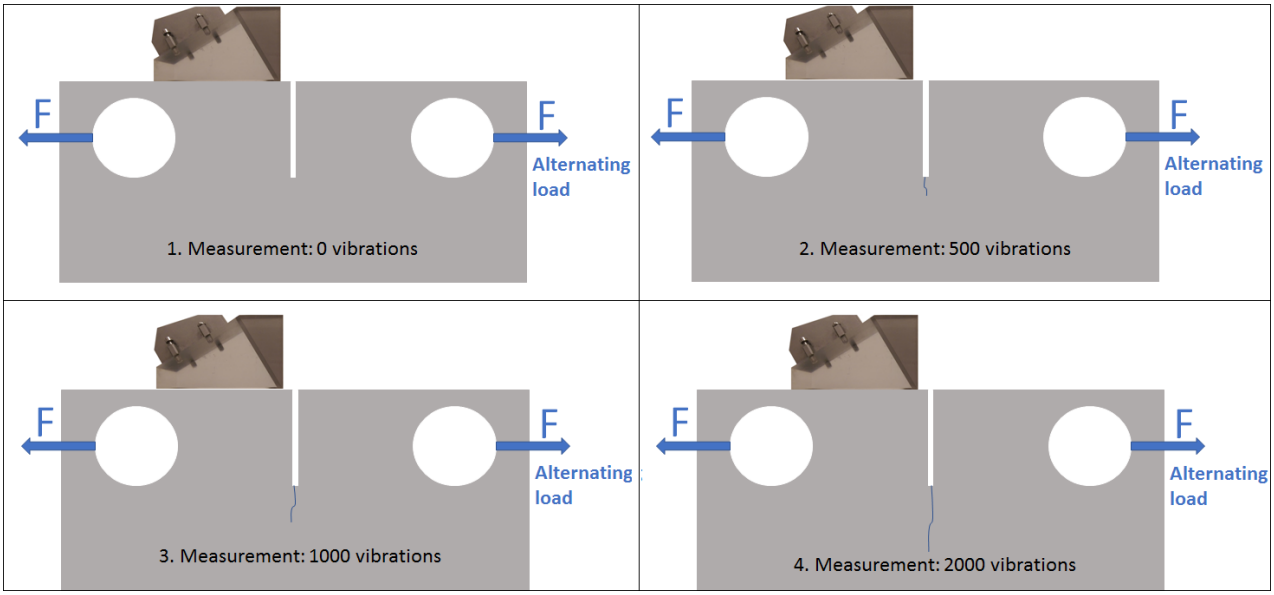

Figure 38: Schematic illustration of alternating loads applied to an aluminum CT specimen in order to increasingly develop a fatigue crack.

crack and for $d_1 = 4mm$ the detection of the crack tip seemed unclear whereas for $d_1 = 4.2mm$ and $4.4mm$ a clear trend of the crack tip could be observed.

The results clearly demonstrate the efficiency of the presented method to detect and image nonlinear defects. However, to further test and evaluate this method, other experiments can be done in prospective research. In this research, the force for stretching the notches in the specimens was applied mechanically. Since no evaluation of the presented imaging method for monitoring the depth of the crack in the aluminum specimen could be done, it seems interesting to investigate an aluminum CT specimen prepared with a higher thickness such that the vertical growth of the crack can be analyzed. For this purpose, the force for stretching the notch should be applied dynamically in form of vibrations. In this way, a fatigue crack growth could be slowly developed and examined with the presented imaging method. An approach of such an experiment is illustrated in Fig. 38.

Also, it is worth trying analyzing aluminum specimen with the presented imaging method by using a higher frequency, e.g. 5 or 10 MHz, to investigate the crack depth.

This approach seems interesting since with a higher amplitude signal nonlinear effects can also be detected.

REFERENCES

[1] Administration, F. A., "de havilland dh-106 comet 1," *http://www.lessonslearned.faa.gov/*.

[2] Akihiro Ouchi, Azusa Sugawara, Y. O. and Yamanaka, K., "Subharmonic phased array for crack evaluation using surface acoustic wave," *Japanese Journal of Applied Physics*, vol. 54, Jun 2015.

[3] An, Y.-K. and Lee, D. J., "Nonlinear ultrasonic fatigue crack detection using a single piezoelectric transducer," *Proc. SPIE*, vol. 9803, Apr 2016.

[4] Aschenbach, J., *Wave Propagation in Elastic Solids - Assessment of Stress*. North-Holland, 1999.

[5] Azusa Sugawara, Kentaro Jinno, Y. O. and Yamanaka, K., "Closed-crack imaging and scattering behavior analysis using confocal subharmonic phased array," *Japanese Journal of Applied Physics*, vol. 54, Jun 2015.

[6] Bermes, C., "Generation and detection of nonlinear lamb waves for the characterization of material nonlinearities," Master's thesis, Georgia Institute of Technology, Atlanta, GA, USA, 12 2006.

[7] Drinkwater, B. W. and Wilcox, P. D., "Ultrasonic arrays for non-destructive evaluation: A review," *Ndt & E International*, vol. 39, no. 7, pp. 525–541, 2006.

[8] Ehrlich, C., "Experimental characterization of creep damage using the nonlinearity ultrasonic technique," Master's thesis, Georgia Institute of Technology, Atlanta, GA, USA, 12 2011.

[9] Forstenhaeusler, M., "Nonlinear resonance ultrasonic spectroscopy for characterizing thermal damage in 17-4ph stainless steel," Master's thesis, Georgia Institute of Technology, Atlanta, GA, USA, 12 2016.

[10] Green, A., "A general theory of an elastic-plastic continuum," *Archive for Rational Mechanics and Analysis*, vol. 18, p. 251, 1965.

[11] Gruen, D., "Numerical analysis of intragrain precipitate influence on the linear scattering behavior," Master's thesis, Georgia Institute of Technology, Atlanta, GA, USA, 12 2016.

[12] Herrmann, J., "Generation and detection of higher harmonics in rayleigh waves using laser ultrasound," Master's thesis, Georgia Institute of Technology, Atlanta, GA, USA, 2005.

[13] Jin-Yeon Kim, J. L., "Experimental characterization of fatigue damage in a nickel-based super alloy using nonlinear ultrasonic waves," *Journal of the Acoustical Society of America*, vol. 120, p. 1266, 2006.

[14] Jingwei Cheng, Jack N Potter, A. J. C. and Drinkwater, B. W., "Monitoring fatigue crack growth using nonlinear ultrasonic phased array imaging," *Smart Mater. Struct.*, vol. 26, Mar 2017.

[15] Lester W., S. J., *Fundamentals of Ultrasonic Phased Arrays*. Switzerland: Springer, 2015.

[16] Marino, D., "Using nonlinear ultrasound measurements to assess the stage of thermal damage in modified 9thesis, Georgia Institute of Technology, Atlanta, GA, USA, 12 2014.

[17] Mark F. Hamilton, D. T. B., *Nonlinear Acoustics*. Academic Press, 1998.

[18] Masako Ikeuchi, Kentaro Jinno, Y. O. and Yamanaka, K., "Improvement of closed crack selectivity in nonlinear ultrasonic imaging using fundamental wave amplitude difference," *Japanese Journal of Applied Physics*, vol. 52, Jul 2013.

[19] Matlack, K., K. J.-Y. J. L. and Qu, J., "Review of second harmonic generation measurement techniques for material state determination in metals," *Journal of Nondestructive Evaluation*, vol. 34, pp. 1–23, 2015.

[20] Morlock, F., "Evaluation of stress corrosion cracking in sensitized 304 stainless steel using nonlinear rayleigh waves," Master's thesis, Georgia Institute of Technology, Atlanta, GA, USA, 12 2014.

[21] Norris, A., "Symmetry conditions for third order elastic moduli and implications in nonlinear wave theory," *Journal of Elasticity*, vol. 25, pp. 247 – 257, 1991.

[22] Olympus, "Conventional transducer construction," *http://www.olympus-ims.com/en/ndt-tutorials/transducers/construction/*.

[23] Olympus, "Ndt - tutorials," *http://www.olympus-ims.com/en/ndt-tutorials/instrumententation/bscan/*.

[24] Olympus, "Omniscan - mx2," *http://www.olympus-ims.com/de/omniscan-mx2/*.

[25] Pietro Burrascano, Sergio Callegari, A. M. M. R. M. V., *Ultrasonic Nondestructive Evaluation Systems - Industrial Application Issues*. Switzerland: Springer, 2015.

[26] Potter, J. N., Croxford, A. J., and Wilcox, P. D., "Nonlinear ultrasonic phased array imaging," *Phys. Rev. Lett.*, vol. 113, p. 144301, Oct 2014.

[27] Pruell, C., K. J.-Y. Q. J. and Jacobs, L., "A nonlinear-guided wave technique for evaluating plasticity-driven material damage in a metal plate," *Ndt & E International*, vol. 42, pp. 199–203, 2009.

[28] Romer, A., "The second harmonic generation in reflection mode - an analytical, numerical and experimental study," Master's thesis, Georgia Institute of Technology, Atlanta, GA, USA, 12 2014.

[29] Tech, R., *Introduction to Phased Array Ultrasonic Technology Applications*. R/D Tech, 2007.

[30] Walker, S. V., K.-J.-Y. Q. J. and Jacobs, L. J., "Fatigue damage evaluation in a36 steel using nonlinear rayleigh surface waves," *Ndt & E International*, vol. 48, pp. 10–15, 2012.

[31] Yoshikazu Ohara, Taro Oshiumi, H. N. K. Y. X. W. T. U. T. T. T. T. and Mihara, T., "Ultrasonic phased array with surface acoustic wave for imaging cracks," *AIP Advances*, vol. 7, Jun 2017.

[32] Yoshikazu Ohara, Yohei Shintaku, M. H. S. H. and Yamanaka, K., "Fundamental study on nonlinear ultrasonic imaging method for closed cracks using subtraction of responses at different external loads," *20. International Congress on Acoustics*, 2010.

[33] Yoshikazu Ohara, Tsuyoshi Mihara, R. S. T. O. S. Y. Y. K. and Yamanaka, K., "Imaging of closed cracks using nonlinear response of elastic waves at subharmonic frequency," *Applied Physics Letters*, vol. 25, pp. 247 – 257, Jan 2007.

[34] Yoshikazu Ohara, Koji Takahashi, Y. I. K. Y. and Mihara, T., "Imaging of closed cracks in coarse-grained materials by nonlinear ultrasonic phased array," *Proceedings of Symposium on Ultrasonic Electronics*, vol. 36, Nov 2015.